3

Time Domain Adaptive Integral Method for Surface Integral Equations

H. Bağcı, A.E. Yılmaz, J.-M. Jin, and E. Michielssen

3.1 Introduction

To ensure the interoperability of modern broadband and integrated navigation and communication systems, engineers need simulation tools capable of tracking electromagnetic transients on electrically large and complex, multiscale and potentially nonlinearly loaded structures. In this context, marching-on-in-time based time-domain integral-equation (MOT-TDIE) solvers provide an increasingly appealing alternative to finite difference/element based simulation engines [1, 2]. Indeed, compared to the latter, MOT-TDIE solvers automatically impose radiation conditions, do not require fields to be discretized throughout homogeneous volumes, and are highly immune to numerical dispersion [3, 4]. Moreover, recent algorithmic advances have rendered these solvers (a) well-conditioned and stable, (b) computationally efficient, and (c) applicable to the analysis transients on geometrically complex structures. (d) Finally, MOT-TDIE solvers have been hybridized with various subsystem simulators, thereby vastly expanding their application range.

1. *Stability and conditioning:* Modern MOT-TDIE solvers, in contrast to their predecessors, are (almost always) stable. Indeed, during the past decade, the stability of these solvers has steadily improved due to the application of averaging/filtering techniques [5, 6], implicit time stepping methods [7, 8], smooth and carefully tailored temporal basis functions [7, 9, 10], and space-time Galerkin schemes [11]. Recently, time-domain Calderón identities [12] and spatially-hierarchical schemes [13] were leveraged to precondition MOT-TDIE systems, thereby accelerating the convergence of their iterative solution. These developments have enabled the robust application of MOT-TDIE solvers to the analysis of transients on structures modeled in terms of high-density/multiscale unstructured meshes.
2. *Acceleration algorithms:* The computational complexity and memory requirements of classical MOT-TDIE solvers scale very poorly. To remedy

this solution, two accelerators were developed: the (multilevel) plane wave time-domain algorithm (PWTD) [14–16] and the time-domain adaptive integral method (TD-AIM) [17]. These accelerators permit the rapid evaluation of transient fields due to wideband source constellations, viz. the fast computation of all space-time convolutions required by MOT-TDIE solvers, thereby have enabled the MOT-TDIE analysis of transients on structures involving in excess of one million spatial basis functions lasting thousands of time steps, and this on readily available parallel computers.

3. *Complex structures:* Modern MOT-TDIE solvers, unlike their predecessors which target simple perfect electrically conducting (PEC) structures, apply to the analysis of electromagnetic transients on surfaces characterized by impedance boundary conditions [18], surfaces buried in half-space backgrounds [19, 20], dielectric/lossy/dispersive penetrable volumes [21–23], and surfaces with wire attachments [24, 25]. These solvers permit modeling of electromagnetic transients on real-world structures, e.g., complex platform-mounted and dielectric backed antennas and their feeds, and quasi-optical devices.
4. *Hybridization with subsystem simulators:* Whereas historically MOT-TDIE solvers were used primarily as stand-alone electromagnetic analysis engines, recently they have been hybridized with various subsystem simulators including circuit and [26, 27] cable solvers [25, 28–31], and macromodeling tools [32]. This hybridization has rendered MOT-TDIE solvers useful for analyzing field interactions with platforms carrying cable-interconnected circuits, electronic components, and printed circuit boards.

Without a doubt, fast MOT-TDIE solver technology is rapidly approaching a stage of maturity permitting its widespread application to complex and real-world engineering problems. This chapter summarizes some of the authors' recent work in the field, much of which is rooted in the work of J.C. Nédélec and co-workers [11, 33, 34]. Specifically, it describes recent progress in the formulation and implementation of TD-AIM accelerated MOT-TDIE solvers, viz. extensions of the frequency-domain adaptive integral method (AIM) [35] and pre-corrected FFT algorithm [36] to the time domain, and demonstrates the technology's applicability to a host of real-world electromagnetic interference (EMI) problems.

The remainder of the chapter is organized as follows. Section 3.2 introduces the reader to FFT-accelerated MOT-TDIE solvers by contrasting the technology to FFT-accelerated frequency-domain and PWTD-accelerated time-domain solvers. Section 3.3 describes several time-domain surface integral equations, outlines classical MOT schemes for solving them, and describes the TD-AIM accelerator (including its parallel implementation). Section 3.4 elucidates the hybridization of TD-AIM-accelerated MOT-TDIE solvers with several subsystem simulators and demonstrates the versatility of the resulting hybrid simulators through their application to several real-world EMI problems.

3.2 FFT-Accelerated MOT-TDIE Solvers: A Perspective

The aforementioned PWTD scheme constitutes the extension of the Helmholtz-equation fast multipole scheme [37–40] to the time domain. Its development preceded that of the TD-AIM discussed here. How do these schemes compare and why is there a need for a second accelerator? This section answers some of these questions and places the development of the TD-AIM into its historical perspective.

FFT schemes for accelerating the solution of frequency-domain (time-harmonic) integral equations, such as the conjugate gradient FFT (CG-FFT) method [41], frequency-domain AIM [35], and pre-corrected FFT algorithm [36], provide an appealing avenue for tackling a broad class of surface scattering problems. The classical iterative solution of frequency-domain integral equations requires $O\left(N_{\mathrm{s}}^2\right)$ operations per matrix-vector multiplication and $O\left(N_{\mathrm{s}}^2\right)$ bytes of memory; here, and in what follows, N_{s} denotes the number of spatial basis functions that discretize the scatterer current density. Both the CG-FFT algorithm and AIM reduce the computational complexity of a matrix-vector multiplication by employing uniform spatial grids that facilitate the use of (spatial) FFTs for rapidly convolving source distributions with Green functions. To this end, the CG-FFT algorithm assumes a uniform scatterer discretization, whereas the AIM introduces a uniform auxiliary grid that does not constrain the primary surface discretization. The AIM reduces the above matrix-vector multiplication cost to $O\left(N_{\mathrm{c}} \log N_{\mathrm{c}}\right)$ operations and the associated memory requirements to $O\left(N_{\mathrm{c}}\right)$ bytes, where N_{c} is the number of nodes of the auxiliary grid. For general three-dimensional (3D) surfaces devoid of geometric details, $N_{\mathrm{c}} \sim N_{\mathrm{s}}^{1.5}$; for quasi-planar surfaces whose transverse dimensions are much larger than their (fixed) height, $N_{\mathrm{c}} \sim N_{\mathrm{s}}$. The computational complexity and memory requirements of AIM-accelerated solvers generally scale less favorably than those of multilevel fast multipole ones [39, 40]. Nonetheless, the AIM often remains a viable alternative, especially when the structure under study is relatively small, quasi-planar, or densely packed. The AIM also has the advantage of being immediately applicable to all problems involving Green functions that exhibit translational, rotational, or reflection invariance [40]. Recently proposed higher-order methods [42, 43], which employ auxiliary uniform grids on facets to reduce N_{c}, and effective parallelization strategies based on either domain decomposition [35] or parallel spatial FFTs [44] further improve the viability of AIM-like solvers for large-scale frequency-domain analysis.

The above picture carries over virtually entirely to the time domain. The classical MOT solution of TDIEs requires $O\left(N_{\mathrm{t}} N_{\mathrm{s}}^2\right)$ operations and $O\left(N_{\mathrm{s}}^2\right)$ bytes of memory; here N_{t} is the number of time steps in the simulation. Recently, various extensions of the CG-FFT algorithm to the time domain have been proposed [45–48]. Similar to their frequency-domain counterpart, these algorithms assume a uniform discretization of the scatterer surface and therefore are of limited use. This chapter describes the TD-AIM, i.e., the

time-domain counterpart of the AIM; its predecessors and related methods were outlined in [35, 49–53]. The TD-AIM has computational complexity and memory requirements of $O\left(N_{\mathrm{t}}N_{\mathrm{c}}\left(\log N_{\mathrm{c}}+\log^2 N_{\mathrm{g}}\right)\right)$ and $O\left(N_{\mathrm{g}}N_{\mathrm{c}}\right)$, respectively. Here, N_{g} denotes the maximum number of time steps for a pulsed field to travel across the scatterer; for surface scatterers, N_{g} is generally proportional to $N_{\mathrm{s}}^{0.5}$ [48]. TD-AIM attains these efficiency gains by accelerating the field computations as briefly described next and detailed in Sect. 3.3:

1. All space-time sources on the scatterer surface, which produce transient fields, are locally projected onto a uniform auxiliary grid for each time step.
2. The fields due to the resulting auxiliary-grid sources are computed everywhere on the grid via global, multilevel/blocked, space-time FFTs.
3. These fields are locally interpolated back onto the scatterer surface.
4. As this procedure is inaccurate when source and observer points reside close to each other, near fields are computed classically and (pre-) corrected for errors introduced through the use of global FFTs.

Just as the frequency-domain AIM is asymptotically less efficient than the multilevel fast multipole method, the TD-AIM is asymptotically inferior to the multilevel PWTD scheme. That said, as the TD-AIM relies solely on the translational invariance of the Green function to achieve computational savings, it is applicable with little modification to problems involving lossy [53], layered [19, 20], or dispersive media [54]. Furthermore, as subsequent sections will show, it is relatively easy to implement and parallelize. Finally, TD-AIM accelerated MOT-TDIE solvers trivially lend themselves to hybridization with various subsystem simulators. In conclusion, for many problems of practical interest, the TD-AIM is computationally efficient and effective; the method is an attractive alternative to the PWTD algorithm.

3.3 FFT-Accelerated MOT-TDIE Solvers: Formulation and Implementation

This section details the construction of FFT-accelerated MOT-TDIE solvers. First, time-domain electric-, magnetic-, and combined-field integral equations for analyzing electromagnetic scattering from PEC structures residing in an unbounded homogenous medium are presented and their classical MOT-based solution is reviewed. Next, the TD-AIM is introduced and its theoretical computational complexity and memory requirements are explored. Also, a parallel implementation of the scheme is described. The section concludes by describing numerical experiments that demonstrate the accuracy and parallel efficiency of the TD-AIM accelerated MOT-TDIE solver.

3.3.1 Time-Domain Integral Equations and Their Solution via Marching-on-fin-Time

Let S denote the surface of a closed PEC body that resides in an unbounded, lossless, homogenous dielectric medium with permittivity ε and permeability μ. A transient electromagnetic field $\left\{\mathbf{E}^{\text{inc}}(\mathbf{r},t),\ \mathbf{H}^{\text{inc}}(\mathbf{r},t)\right\}$ is incident on S; it is assumed that this field is (approximately) temporally bandlimited to $f_{\max}$ and that it vanishes $\forall \mathbf{r} \in S$ for $t < 0$. A surface current is induced on S that in turn generates the scattered field

$$\mathbf{E}^{\text{sca}}(\mathbf{r},t) = -\partial_t \mathbf{A}(\mathbf{r},t) - \nabla \Phi(\mathbf{r},t), \tag{3.1a}$$

$$\mathbf{H}^{\text{sca}}(\mathbf{r},t) = \nabla \times \mathbf{A}(\mathbf{r},t)/\mu, \tag{3.1b}$$

where ∂_t represents the time derivative and $\mathbf{A}(\mathbf{r},t)$ and $\Phi(\mathbf{r},t)$ are the vector and scalar potentials

$$\mathbf{A}(\mathbf{r},t) = \mu \iint_S \frac{\mathbf{J}(\mathbf{r}', t - R/c)}{4\pi R}\, \mathrm{d}s', \tag{3.2a}$$

$$\Phi(\mathbf{r},t) = -\frac{1}{\varepsilon} \iint_S \int_0^{t-R/c} \frac{\nabla' \cdot \mathbf{J}(\mathbf{r}', t')}{4\pi R}\, \mathrm{d}t' \mathrm{d}s'. \tag{3.2b}$$

Here, $\mathbf{J}(\mathbf{r},t)$ is the surface current density, $R = |\mathbf{r} - \mathbf{r}'|$ is the distance between source point $\mathbf{r}'$ and observation point $\mathbf{r}$, and $c = 1/\sqrt{\mu\varepsilon}$ is the speed of light. Enforcing the temporal derivatives of the fundamental boundary conditions on the electric and magnetic fields tangential to S yields time-domain electric- and magnetic-field integral equations (EFIE and MFIE). The combined-field integral equation (CFIE) is a linear combination of the EFIE and the MFIE [55, 56]. The time-domain EFIE, MFIE, and CFIE read

$$\begin{aligned} \text{EFIE}: \quad & -\hat{\mathbf{n}}(\mathbf{r}) \times \left(\hat{\mathbf{n}}(\mathbf{r}) \times \partial_t \mathbf{E}^{\text{inc}}(\mathbf{r},t)\right) = \\ & -\hat{\mathbf{n}}(\mathbf{r}) \times \left(\hat{\mathbf{n}}(\mathbf{r}) \times \left(\partial_t^2 \mathbf{A}(\mathbf{r},t) + \nabla \partial_t \Phi(\mathbf{r},t)\right)\right), \end{aligned} \tag{3.3a}$$

$$\begin{aligned} \text{MFIE}: \quad & \hat{\mathbf{n}}(\mathbf{r}) \times \partial_t \mathbf{H}^{\text{inc}}(\mathbf{r},t) = \\ & \partial_t \mathbf{J}(\mathbf{r},t) - \hat{\mathbf{n}}(\mathbf{r}) \times \nabla \times \partial_t \mathbf{A}(\mathbf{r},t)/\mu, \end{aligned} \tag{3.3b}$$

$$\text{CFIE}: \quad \text{CFIE} = \eta(1-\alpha)\,\text{MFIE} + \alpha \text{EFIE}. \tag{3.3c}$$

Here, $\hat{\mathbf{n}}(\mathbf{r})$ is an outward directed unit vector normal to S and $\eta = \sqrt{\mu\varepsilon}$ is the intrinsic impedance of the medium. The discussions hereafter will focus on the CFIE; equations pertaining to the EFIE and the MFIE can be derived from those for the CFIE by setting $\alpha = 1$ and $\alpha = 0$, respectively. The EFIE is valid for open surfaces as well, whereas the MFIE and the CFIE are pertinent to closed surfaces.

To numerically solve the CFIE, $\mathbf{J}(\mathbf{r},t)$ is discretized using $N_\mathrm{s}N_\mathrm{t}$ spatio-temporal basis functions as

$$\mathbf{J}(\mathbf{r},t) \cong \sum_{k'=1}^{N_\mathrm{s}} \sum_{l'=1}^{N_\mathrm{t}} I_{k',l'} \mathbf{S}_{k'}(\mathbf{r})\, T(t - l'\Delta t). \tag{3.4}$$

Here $I_{k',l'}$ is an unknown expansion coefficient and $\Delta t = \beta / f_{\max}$ is the time-step size with typically $0.02 \leq \beta \leq 0.1$. In what follows, the spatial and temporal basis functions $\mathbf{S}_{k'}(\mathbf{r})$ and $T(t)$ are assumed local. For example, the $\mathbf{S}_{k'}(\mathbf{r})$ and $T(t)$ can be Rao–Wilton–Glisson (RWG) functions [57] or their higher-order extensions [58] and shifted Lagrange interpolants [7], respectively. Furthermore, it is assumed that $T(t) = 0$ for $t \leq -\Delta t$ and $t > T^{\max}$, i.e., that the temporal basis functions are (discretely) causal and of duration $T^{\max} + \Delta t$. Finally, spatial discretization lengths on S are assumed to be of $O(c\Delta t)$; this assumption is valid whenever S is electrically large and devoid of small geometric details. Upon substituting (3.4) into the CFIE (3.3c) and testing the resulting equation with the spatial functions $\mathbf{S}_k(\mathbf{r})$ at times $t = l\Delta t$, $N_\mathrm{s}N_\mathrm{t}$ equations for the $N_\mathrm{s}N_\mathrm{t}$ expansion coefficients result:

$$\mathbf{Z}_0 \mathbf{I}_l = \mathbf{V}_l^{\mathrm{inc}} - \mathbf{V}_l^{\mathrm{scat}} = \mathbf{V}_l^{\mathrm{inc}} - \sum_{l'=\max(1,l-N_\mathrm{g})}^{l-1} \mathbf{Z}_{l-l'} \mathbf{I}_{l'} \text{ for } l = 1, 2, \ldots, N_\mathrm{t}. \tag{3.5}$$

The entries of the vectors $\mathbf{I}_{l'}$ and $\mathbf{V}_l^{\mathrm{inc}}$ and those of the matrices $\mathbf{Z}_{l-l'}$ are

$$\mathbf{I}_{l'}(k') = I_{k',l'}, \tag{3.6a}$$

$$\mathbf{V}_l^{\mathrm{inc}}(k) = \iint_S \eta(1-\alpha)\, \mathbf{S}_k(\mathbf{r}) \cdot \hat{\mathbf{n}}(\mathbf{r}) \times \partial_t \mathbf{H}^{\mathrm{inc}}(\mathbf{r},t) + \alpha \mathbf{S}_k(\mathbf{r}) \cdot \partial_t \mathbf{E}^{\mathrm{inc}}(\mathbf{r},t)\, \mathrm{d}s \Big|_{t=(l-l')\Delta t}, \tag{3.6b}$$

$$\begin{aligned} \mathbf{Z}_{l-l'}(k,k') = {} & \eta(1-\alpha) \iint_S \mathbf{S}_k(\mathbf{r}) \cdot \mathbf{S}_{k'}(\mathbf{r}')\ \partial_t T(t)\, \mathrm{d}s \\ & + \eta(1-\alpha) \iint_S (\hat{\mathbf{n}}(\mathbf{r}) \times \mathbf{S}_k(\mathbf{r})) \\ & \times \nabla\mu \iint_S \frac{\partial_t T(t - R/c)\, \mathbf{S}_{k'}(\mathbf{r}')}{4\pi R}\, \mathrm{d}s'\mathrm{d}s \\ & + \alpha \iint_S \mathbf{S}_k(\mathbf{r}) \cdot \mu \iint_S \frac{\partial_t^2 T(t - R/c)\, \mathbf{S}_{k'}(\mathbf{r}')}{4\pi R}\, \mathrm{d}s'\mathrm{d}s \\ & + \alpha \iint_S \nabla \cdot \mathbf{S}_k(\mathbf{r}) \frac{1}{\varepsilon} \iint_S \frac{T(t - R/c)\, \nabla' \cdot \mathbf{S}_{k'}(\mathbf{r}')}{4\pi R}\, \mathrm{d}s'\mathrm{d}s \Big|_{t=(l-l')\Delta t}. \end{aligned} \tag{3.6c}$$

The integer N_g in (3.5) is defined such that $N_\mathrm{g}\Delta t$ approximates the longest possible transit time of the field produced by a temporal basis function across S: $N_\mathrm{g} = \lfloor (R^{\max}/c + T^{\max}) \rfloor$ where $R^{\max}$ is the maximum distance between any two points on S and $\lfloor . \rfloor$ rounds to the smaller integer. It follows that only

the matrices $\mathbf{Z}_0$ through $\mathbf{Z}_{N_g}$ are nonzero because the basis functions are local and the Green function implicit in (3.5) is impulsive in time [53]. That is, the fields radiated by currents on various parts of the scatterer at a given time step interact with the scatterer for at most N_g time steps. Once the spatial and temporal basis functions and the time-step size that support the frequency content of the incident field are determined, the unknown coefficients in (3.5) can be found recursively. First, $\mathbf{I}_1$ at time $t = \Delta t$ is found; this, in turn, permits computation of $\mathbf{V}_2^{\text{scat}}$. This vector is then added to the tested incident field $\mathbf{V}_2^{\text{inc}}$ and (3.5) is solved for the current $\mathbf{I}_2$ at time $t = 2\Delta t$. At the next time step, $\mathbf{I}_1$ and $\mathbf{I}_2$ are used to compute $\mathbf{V}_3^{\text{scat}}$, which together with $\mathbf{V}_3^{\text{inc}}$ permits the computation of $\mathbf{I}_3$, and so forth. This recursive solution algorithm is known as the MOT scheme [59].

The dominant cost of the MOT method is the computation of the vectors $\mathbf{V}_l^{\text{scat}}$, which involves a space-time convolution of the currents with the Green function for each time step l. Indeed, under the above assumptions, for $l > N_g$, that is, as soon as the retarded fields from every part of the scatterer reach all the other parts, the computation of a single $\mathbf{V}_l^{\text{scat}}$ requires $O\left(N_s^2\right)$ operations. Compared to the cost of computing $\mathbf{V}_l^{\text{scat}}$, the cost of iteratively solving (3.5) typically is insignificant because $\mathbf{Z}_0$ contains only $O\left(N_s\right)$ nonzero elements, i.e., it is highly sparse, and the iterative solution typically converges in very few (<15) iterations. Thus, the goal of the TD-AIM is to accelerate the computation of the fields on the right-hand side of (3.5), the classical evaluation of which requires $O\left(N_t N_s^2\right)$ operations for all time steps.

3.3.2 Time Domain Adaptive Integral Method (TD-AIM)

The space-time translational invariance of the Green function inherent in (3.6c) can be exploited to rapidly evaluate $\mathbf{V}_l^{\text{scat}}$ for $1 \leq l \leq N_t$. The scheme presented here is a marriage between the fast time- and frequency-domain integral-equation solvers in [53] and [35]. In [53], a fast scheme for evaluating the temporal convolution of the impedance matrices $\mathbf{Z}_{l-l'}$ with space-time currents was introduced assuming that S was a uniformly meshed plate. Temporal convolutions were evaluated via blocked (multilevel) FFTs while spatial convolutions could be evaluated by a CG-FFT like scheme because of the uniform surface mesh used. In [35], a fast scheme for evaluating fields generated by time-harmonic sources residing on an arbitrarily shaped and meshed surface was described. The use of FFTs to evaluate these fields was facilitated by introducing an auxiliary grid. Here, the extension of the scheme in [53] to nonuniformly meshed surfaces using ideas similar to [35] is elucidated.

The TD-AIM embeds S within an auxiliary 3D Cartesian grid with $N_c = N_{cx} \times N_{cy} \times N_{cz}$ nodes. Node separation along the three Cartesian directions Δs_x, Δs_y, and Δs_z are assumed identical and equal to Δs for ease of presentation; the effects of node separation on accuracy are investigated in Sect. 3.3.6 but Δs is always of $O(c\Delta t)$. The TD-AIM computes $\mathbf{V}_l^{\text{scat}}$ in four stages:

1. At each time step, all primary sources on S are locally projected onto the auxiliary grid. The auxiliary sources that are associated with a given primary source are chosen to reproduce the transient fields of the primary source with high accuracy, at least for observation points that are separated by more than a pre-specified distance from the primary source.
2. Future transient fields produced by these auxiliary sources are computed at all the nodes on the auxiliary grid; this is achieved via global, blocked, space-time FFTs.
3. The fields at the next time step are locally interpolated from the auxiliary grid onto the primary surface mesh.
4. Near fields due to all primary sources on S are computed wherever needed and (pre-) corrected for errors induced through the use of global FFTs in Stage (2).

Specifically, the TD-AIM approximates each of the impedance matrices $\mathbf{Z}_1$ through $\mathbf{Z}_{N_\mathrm{g}}$ as $\mathbf{Z}_{l-l'} \approx \mathbf{Z}_{l-l'}^{\mathrm{FFT}} + \mathbf{Z}_{l-l'}^{\mathrm{near}}$, where $\mathbf{Z}_{l-l'}^{\mathrm{FFT}}$ and $\mathbf{Z}_{l-l'}^{\mathrm{near}}$ account for Stages (1)–(3) and Stage (4) of the algorithm, respectively. The matrices $\mathbf{Z}_{l-l'}^{\mathrm{FFT}}$ can be expressed as

$$\begin{aligned}\mathbf{Z}_{l-l'}^{\mathrm{FFT}} = \; & \eta\,(1-\alpha)\left[\,\boldsymbol{\Gamma}_x^{\dagger}(t)\;\boldsymbol{\Gamma}_y^{\dagger}(t)\;\boldsymbol{\Gamma}_z^{\dagger}(t)\,\right] \\ & * \begin{bmatrix} \mathbf{0} & \mathbf{G}^{Hy}(t) & -\mathbf{G}^{Hz}(t) \\ -\mathbf{G}^{Hx}(t) & \mathbf{0} & \mathbf{G}^{Hz}(t) \\ \mathbf{G}^{Hx}(t) & -\mathbf{G}^{Hy}(t) & \mathbf{0} \end{bmatrix} * \begin{bmatrix} \boldsymbol{\Lambda}_x(t) \\ \boldsymbol{\Lambda}_y(t) \\ \boldsymbol{\Lambda}_z(t) \end{bmatrix} \\ & +\alpha\left[\,\boldsymbol{\Lambda}_x^{\dagger}(t)\;\boldsymbol{\Lambda}_y^{\dagger}(t)\;\boldsymbol{\Lambda}_z^{\dagger}(t)\,\right] * \begin{bmatrix} \mathbf{G}^{A}(t) * \boldsymbol{\Lambda}_x(t) \\ \mathbf{G}^{A}(t) * \boldsymbol{\Lambda}_y(t) \\ \mathbf{G}^{A}(t) * \boldsymbol{\Lambda}_z(t) \end{bmatrix} \\ & +\alpha\boldsymbol{\Lambda}_{\nabla}^{\dagger}(t) * \mathbf{G}^{\varphi}(t) * \boldsymbol{\Lambda}_{\nabla}(t)\Big|_{t=(l-l')\Delta t}, \end{aligned} \tag{3.7}$$

where $\boldsymbol{\Lambda}_{x,y,z,\nabla}(t)$ and $\boldsymbol{\Gamma}_{x,y,z}(t)$ are sparse and time-dependent matricial projection operators, † represents a transpose, $*$ denotes a combined temporal convolution/matrix multiplication, and the matricial $\mathbf{G}^{\mathbf{H},A,\varphi}(t)$ propagate onto all of the auxiliary-grid nodes (temporal derivatives of) magnetic fields, magnetic vector potentials, and electric scalar potentials due to sources on the auxiliary grid. In (3.7), the curl operator of (3.6c) is transferred onto neither the spatial basis functions [60] nor the spatial testing functions [35]; rather, is left on the Green functions to facilitate its numerical computation as described in Sect. 3.3.4 and [61]. The various entities in (3.7) are discussed in more detail below.

The matricial projection operators are constructed by choosing M_k points on the auxiliary grid that each function $\mathbf{S}_k(\mathbf{r})$ is projected onto; denote this set of points by C_k. These points can be chosen to reside inside or on the surface of the smallest cube that snaps to the auxiliary grid and that encloses $\mathbf{S}_k(\mathbf{r})$. Then, for each $\mathbf{S}_k(\mathbf{r})$, the M_k entries of the seven matricial projection

operators $\mathbf{\Lambda}_{x,y,z,\nabla}(t)$ and $\mathbf{\Gamma}_{x,y,z}(t)$ are selected such that the scalar fields produced by $\hat{\mathbf{x}} \cdot \mathbf{S}_k(\mathbf{r}) T(t)$, $\hat{\mathbf{y}} \cdot \mathbf{S}_k(\mathbf{r}) T(t)$, $\hat{\mathbf{z}} \cdot \mathbf{S}_k(\mathbf{r}) T(t)$, $\nabla \cdot \mathbf{S}_k(\mathbf{r}) T(t)$, $\hat{\mathbf{x}} \cdot \hat{\mathbf{n}}(\mathbf{r}) \times \mathbf{S}_k(\mathbf{r}) T(t)$, $\hat{\mathbf{y}} \cdot \hat{\mathbf{n}}(\mathbf{r}) \times \mathbf{S}_k(\mathbf{r}) T(t)$, and $\hat{\mathbf{z}} \cdot \hat{\mathbf{n}}(\mathbf{r}) \times \mathbf{S}_k(\mathbf{r}) T(t)$, "match" those of the auxiliary sources for observers separated from the $\mathbf{S}_k(\mathbf{r})$ by several grid lengths Δs.

Two of the most commonly used criteria in determining the auxiliary source amplitudes in frequency-domain AIM are moment matching [35] and field matching [62]. The field-matching approach often results in better accuracy with little extra cost. The two approaches differ significantly, however, when applied in a TD-AIM framework.

In the moment-matching approach, the auxiliary source strengths and temporal signatures are chosen to reproduce the M_k multipole moments of the original basis function. Because the moments are frequency independent, the temporal signatures of the equivalent sources coincide with those of the temporal basis functions. Moreover, because the temporal basis functions are, in general, zero at sampling instants (except at $t = 0$), all $*$ operations in (3.7) reduce to matrix multiplications. While the resulting coefficients are frequency independent, the accuracy of the representation is frequency dependent.

In the field-matching approach, the coefficients and time signatures of the auxiliary sources are chosen to replicate the transient fields radiated by the original basis function on a near-field sphere. To this end, the discrete Fourier transform of the radiated field is computed at a set of frequencies, and at each of these frequencies the coefficients are found via least-squares approximation. Then, samples of $\mathbf{\Lambda}_{x,y,z,\nabla}(t)$ and $\mathbf{\Gamma}_{x,y,z}(t)$ are found by inverse discrete Fourier transformation. Because the best-fit coefficients are frequency-dependent, the temporal signatures of the auxiliary sources may differ from basis function to basis function and from auxiliary source point to auxiliary source point. In addition, they are, in general, nonzero at sampling instants. While the coefficients are frequency dependent, the accuracy of the representation can potentially be made frequency independent.

Although the field-matching approach usually produces more accurate results for a given $M_{k'}$, moment matching is more suitable for practical applications because it (a) automatically yields time-limited $\mathbf{\Lambda}_{x,y,z,\nabla}(t)$ and $\mathbf{\Gamma}_{x,y,z}(t)$, (b) allows more matrix-elements to be approximated accurately via (3.7) (see below), and (c) needs fewer operations for multiplying $\mathbf{Z}^{\mathrm{FFT}}_{l-l'}$.

In (3.7), the entries of the sparse propagation matricial $\mathbf{G}^{\mathbf{H},A,\varphi}(t)$ are

$$\left\{\mathbf{G}^{Hx}(t,u,u'), \mathbf{G}^{Hy}(t,u,u'), \mathbf{G}^{Hz}(t,u,u'), \mathbf{G}^{A}(t,u,u'), \mathbf{G}^{\varphi}(t,u,u')\right\} \tag{3.8}$$

$$= \left\{\mu\partial_x\partial_t, \mu\partial_y\partial_t, \mu\partial_z\partial_t, \mu\partial_t^2, 1/\varepsilon\right\} \frac{\delta(t - |\mathbf{r} - \mathbf{r}_{u'}|/c)}{4\pi|\mathbf{r} - \mathbf{r}_{u'}|}\bigg|_{\mathbf{r}=\mathbf{r}_u}. \tag{3.9}$$

where $\mathbf{r}_u$ denotes node u on the auxiliary grid. Note that, to avoid singularities, $\mathbf{G}^{\mathbf{H},A,\varphi}(t,u,u') \equiv 0$. The efficient action of these matricial propagators on equivalent source signatures via blocked FFTs is discussed in Sect. 3.3.3.

The M_k point sources on the auxiliary grid can accurately reproduce the transient fields of $\mathbf{S}_k(\mathbf{r})$ only for observers separated from the source by several grid lengths Δs. Their erroneous contributions to the fields at nearby observers are corrected with the help of $\mathbf{Z}_{l-l'}^{\text{near}}$ matrices. The matrices $\mathbf{Z}_{l-l'}^{\text{near}}$ are sparse approximations to $\mathbf{Z}_{l-l'} - \mathbf{Z}_{l-l'}^{\text{FFT}}$ and are defined as

$$\mathbf{Z}_{l-l'}^{\text{near}}(k,k') = \begin{cases} 0 & \text{if } R_{k,k'} > \gamma\Delta s, \\ \mathbf{Z}_{l-l'}(k,k') - \mathbf{Z}_{l-l'}^{\text{FFT}}(k,k') & \text{if } R_{k,k'} \leq \gamma\Delta s, \end{cases} \tag{3.10}$$

where, $R_{k,k'}$ is the minimum "grid-distance" between the auxiliary points representing the functions $\mathbf{S}_k(\mathbf{r})$ and $\mathbf{S}_{k'}(\mathbf{r})$ [35], i.e.,

$$\begin{aligned} R_{k,k'} &= \min_{u \in C_k, u' \in C_{k'}} \|\mathbf{r}_u - \mathbf{r}_{u'}\|_\infty \\ &= \min_{u \in C_k, u' \in C_{k'}} \max\left(|x_u - x_{u'}|, |y_u - y_{u'}|, |z_u - z_{u'}|\right), \end{aligned} \tag{3.11}$$

and $\gamma\Delta s$ is a threshold distance beyond which $\mathbf{Z}_{l-l'}^{\text{FFT}}$ represents the scattered fields with the desired accuracy; in practice, $1 \leq \gamma \leq 6$. In general, the larger γ is the more costly and the more accurate the TD-AIM becomes.

3.3.3 Multilevel/Blocked Space–Time FFTs

In practice, the entries of the matrices $\mathbf{Z}_{l-l'}^{\text{FFT}}$ defined above are never evaluated. Rather, discrete convolutions of the form

$$\sum_{l'=\max(1,l-N_{\text{g}})}^{l-1} \mathbf{Z}_{l-l'}^{\text{FFT}} \mathbf{I}_{l'} \tag{3.12}$$

are evaluated by discretizing the temporal convolutions inherent in (3.7). It then becomes clear that Stage (2) of the TD-AIM calls for the evaluation of discrete convolutions of the form

$$\sum_{l'=\max(1,l-N_{\text{g}})}^{l-1} \mathbf{G}_{l-l'}^{\mathbf{H},A,\varphi} \tilde{\mathbf{I}}_{l'}^{\mathbf{H},A,\varphi}. \tag{3.13}$$

Here $\mathbf{G}_{l-l'}^{\mathbf{H},A,\varphi} = \mathbf{G}^{\mathbf{H},A,\varphi}(t) * \tilde{T}(t)\Big|_{t=(l-l')\Delta t}$ and $\tilde{T}(t)$ is a function that interpolates the auxiliary source samples $\tilde{\mathbf{I}}_{l'}^{\mathbf{H},A,\varphi}$ (typically, although not necessarily, $\tilde{T}(t) = T(t)$). The FFT-acceleration scheme for evaluating these discrete temporal convolutions exploits the spatial Toeplitz structure of the above operators as well as that of their temporal arrangement implicit in (3.5) to accelerate these multiplications via blocked four-dimensional (4D) FFTs. In what follows, the mechanics of this operation are demonstrated; for the sake of brevity, only scalar potential contributions are considered.

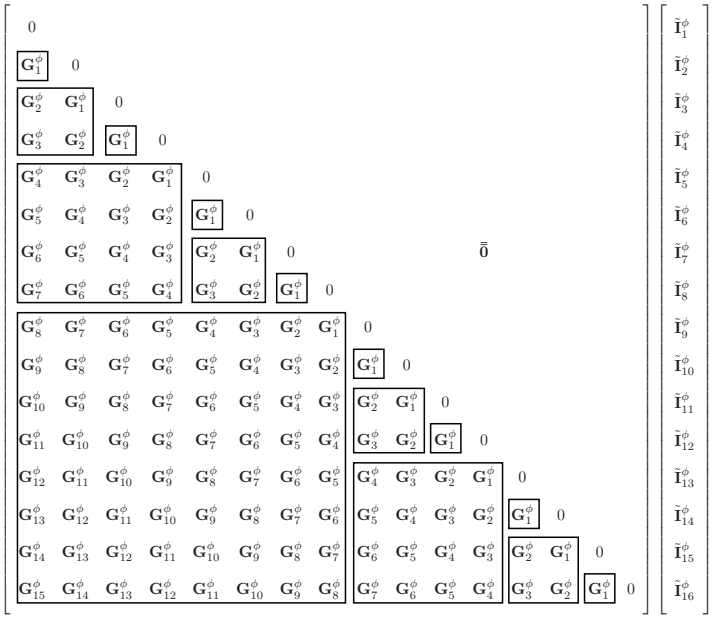

Fig. 3.1. Computation of the scalar potential contribution in (3.13). At each time step l, row l of the matrix-vector multiplication has to be computed. Rather than computing the multiplication row-by-row as in the MOT method, one of the blocked aggregates indicated by *squares* is multiplied at each time step. Causality is not violated: only past currents are used to find the present and future fields

To our knowledge, the use of space–time FFTs for solving time-domain integral equations was first proposed in the context of a global solution scheme, i.e., one that does not march in time but instead solves for all space–time unknowns simultaneously [45]. Nevertheless, space–time FFTs can also be used while marching in time by employing the multilevel/blocking framework of [48] or [53]; the latter was originally proposed in [63]. In this chapter, the scheme of [53] is adopted because of its simplicity. Figure 3.1 illustrates the mechanics of computing the scalar potential on the auxiliary grid for the first 16 time steps. Denote the matrix in Fig. 3.1 by $\mathbf{G}^{\varphi}$; for future reference, denote the corresponding magnetic field and vector potential matrices by $\mathbf{G}^{\mathbf{H}}$ and $\mathbf{G}^{A}$, respectively. To compute, for example at time step eight, the scalar potentials generated by $\mathbf{J}(\mathbf{r}, t)$ on S, the block matrix comprising the leftmost seven matrices on row eight of $\mathbf{G}^{\varphi}$, i.e., $[\mathbf{G}_7^{\varphi}, \mathbf{G}_6^{\varphi}, \ldots, \mathbf{G}_1^{\varphi}]$, has to be multiplied by the vector $[\tilde{\mathbf{I}}_1^{\varphi\dagger}, \tilde{\mathbf{I}}_2^{\varphi\dagger}, \ldots, \tilde{\mathbf{I}}_7^{\varphi\dagger}]^{\dagger}$. Note that $\mathbf{G}^{\varphi}$ (and its extension to all N_{t} time steps) is block-Toeplitz on four levels; the temporal Toeplitz structure is immediately visible in Fig. 3.1 and the 3D spatial Toeplitz structure of each of the matrices $\mathbf{G}_{l-l'}^{\varphi}$ follows trivially from their construction. Therefore, $\mathbf{G}^{\varphi}$ can be rapidly multiplied by a vector using 4D FFTs. When operating within

an MOT framework, however, the current vectors $\tilde{\mathbf{I}}_8^{\varphi}, \tilde{\mathbf{I}}_9^{\varphi}, \ldots, \tilde{\mathbf{I}}_{N_\mathrm{t}}^{\varphi}$ are unknown at time step seven; moreover, multiplication of the entire $\mathbf{G}^{\varphi}$ by the vector $[\tilde{\mathbf{I}}_1^{\varphi\dagger}, \tilde{\mathbf{I}}_2^{\varphi\dagger}, \ldots, \tilde{\mathbf{I}}_7^{\varphi\dagger}, \tilde{\mathbf{I}}_8^{\varphi\dagger}, \ldots, \tilde{\mathbf{I}}_{N_\mathrm{t}}^{\varphi\dagger}]^\dagger$(with $\tilde{\mathbf{I}}_8^{\varphi}, \tilde{\mathbf{I}}_9^{\varphi}, \ldots, \tilde{\mathbf{I}}_{N_\mathrm{t}}^{\varphi}$ filled with zeros) to compute the scattered fields at time step eight is clearly inefficient (as a similar procedure would have to be repeated each and every time step). Nevertheless, there exist various space–time submatrices of $\mathbf{G}^{\varphi}$ that are themselves block-Toeplitz on four levels and that can be multiplied by current coefficients without violating causality. That is, only currents that are already known are required to multiply these submatrices when marching in time. These submatrices are the aggregates of the individual matrices $\mathbf{G}_{l-l'}^{\varphi}$ indicated by the square boxes superimposed on $\mathbf{G}^{\varphi}$ in Fig. 3.1 and are further referred to as block aggregates. Stage (2) of the TD-AIM computes future scattered fields by multiplying these block aggregates with current vectors.

The cost of multiplying the block aggregates varies from time step to time step. For example, at time step nine, the scheme calls for the multiplication of a block aggregate of size $8N_\mathrm{c} \times 8N_\mathrm{c}$, whereas at time step ten only a matrix of size $N_\mathrm{c} \times N_\mathrm{c}$ is multiplied. Furthermore, larger block aggregates are multiplied less frequently. For example, the $4N_\mathrm{c} \times 4N_\mathrm{c}$ block aggregate in $\mathbf{G}^{\varphi}$ is multiplied only once for every eight time steps, whereas the $N_\mathrm{c} \times N_\mathrm{c}$ block is multiplied once for every two time steps (Fig. 3.1). Using this scheme, future scattered fields are constructed *partially* at each time step, and the *complete* scattered field at a given time step is available only at that time step. That is, at each time step, temporal chunks of past auxiliary current coefficients are transformed to the spectral-frequency domain, multiplied with (the 4D FFTs of) the corresponding block aggregate in Fig. 3.1, and then inverse transformed to produce temporal chunks of future scattered fields.

It is important to note that the largest nonzero block aggregate in $\mathbf{G}^{\varphi}$ contains only $O(N_\mathrm{g})$ block rows and columns. That is, Fig. 3.1 should not be interpreted to imply that the size of the largest block aggregate in $\mathbf{G}^{\varphi}$ scales as $O(N_\mathrm{t})$; indeed, the impulsive nature of the Green function renders the very large block aggregates zero. This implies that the number of different square boxes is only $\lfloor \log_2 N_\mathrm{g} \rfloor + 1$, with the largest one of size $2^{\lfloor \log_2 N_\mathrm{g} \rfloor} N_\mathrm{c} \times 2^{\lfloor \log_2 N_\mathrm{g} \rfloor} N_\mathrm{c}$. Thus, the largest temporal FFT size is proportional not to the duration of the analysis but to the maximum transit time across the scatterer.

3.3.4 Computational Cost and Complexity/Comparison to Other Time Domain Methods

Stages (1), (3), and (4) of the algorithm require $O(N_\mathrm{t} N_\mathrm{s})$ operations because each of the seven projection matricials $\mathbf{\Lambda}_{x,y,z,\nabla}(t)$ and $\mathbf{\Gamma}_{x,y,z}(t)$ as well as each near-field matrix $\mathbf{Z}_{l-l'}^{\mathrm{near}}$ contains at most $O(N_\mathrm{s})$ nonzero elements, and because $\mathbf{Z}_{l-l'}^{\mathrm{near}}$ matrices are zero for $l - l' > l^{\mathrm{near}}$, with $l^{\mathrm{near}} \sim (\gamma \Delta s)/(c\Delta t)$. The sparsity of the projection matrices follows directly from the fact that each basis function $\mathbf{S}_k(\mathbf{r})$ is represented by a fixed number of M_k nodes on

the auxiliary grid where M_k is independent of N_s. That each near-field correction matrix contains no more than $O(N_\mathrm{s})$ nonzero entries and that only a fixed and small number of the $\mathbf{Z}^{\mathrm{near}}_{l-l'}$ matrices are nonzero follows from the following facts: (a) γ is independent of N_s, (b) the temporal functions $\tilde{T}(t)$ are localized, with $c\Delta t$ on the order of the discretization length on S, and (c) the free-space Green function is impulsive in nature. Therefore, each basis function communicates with at most $O(1)$ of its neighbors through the near-field correction matrices. Because the projection and near-field matrices are so sparse, the computational cost of the algorithm is dominated by that of Stage (2), i.e., the multiplication of the matrices $\mathbf{G}^{\mathbf{H},A,\varphi}_{l-l'}$ by vectors of past coefficients of auxiliary sources.

To estimate the computational cost of Stage (2), recall that there are $\lfloor \log_2 N_\mathrm{g} \rfloor + 1$ different nonzero block aggregates in $\mathbf{G}^{\mathbf{H},A,\varphi}$. The ith block aggregate, $i = 0, 1, \ldots, \lfloor \log_2 N_\mathrm{g} \rfloor$, is of size $2^i N_\mathrm{c} \times 2^i N_\mathrm{c}$ and can be multiplied in $O\left(N_\mathrm{c}\left(\log N_\mathrm{c} + 2^i \log 2^i\right)\right)$ operations using space–time FFTs by storing the currents and fields in the spectral domain (k space). Notice that the above complexity estimate is significantly lower than that resulting from a straightforward application of a 4D FFT, which would require $O\left(2^i N_\mathrm{c} \log\left(2^i N_\mathrm{c}\right)\right)$operations. The complexity is reduced by observing that the spatial FFTs need not be repeatedly computed. (This observation is also important for parallel efficiency as discussed in Sect. 3.3.5.) For example, at time step nine, spatial FFTs of auxiliary current coefficients at time steps one through eight are needed, but those of steps one through seven are already computed at previous time steps. Hence, the number of spatial FFTs can be minimized by pre-computing the 3D forward spatial FFTs of each matrix $\mathbf{G}^{\mathbf{H},A,\varphi}_{l-l'}$, by computing 3D forward spatial FFTs of the currents *only* at the previous time step, and by computing 3D inverse spatial FFTs of the fields *only* at the next time step. Because the ith block aggregate is multiplied once every 2^{i+1} time steps, the *per-time step* cost of multiplication is $O\left(N_\mathrm{c}\left(\log N_\mathrm{c}^{0.5^{i+1}} + \log 2^{i/2}\right)\right)$. Thus, the total computational complexity of Stage (2) is

$$N_\mathrm{t} \sum_{i=0}^{\lfloor \log_2 N_\mathrm{g} \rfloor} O\left(N_\mathrm{c}\left(\log N_\mathrm{c}^{0.5^{i+1}} + \log 2^{i/2}\right)\right) = O\left(N_\mathrm{t} N_\mathrm{c}\left(\log N_\mathrm{c} + \lfloor \log_2 N_\mathrm{g} \rfloor^2\right)\right). \tag{3.14}$$

For quasi-planar surfaces, $N_\mathrm{c} \sim N_\mathrm{s}$, while for general 3D surface scatterers $N_\mathrm{c} \sim N_\mathrm{s}^{1.5}$. Therefore, because $N_\mathrm{g} \sim N_\mathrm{s}^{0.5}$, the total number of operations of TD-AIM scales as $O\left(N_\mathrm{t} N_\mathrm{s} \log^2 N_\mathrm{s}\right)$ for quasi-planar surfaces and as $O\left(N_\mathrm{t} N_\mathrm{s}^{1.5} \log^2 N_\mathrm{s}\right)$ for general surfaces. The memory requirements of the TD-AIM is dictated by the largest block to be FFTed, which requires $O(N_\mathrm{g} N_\mathrm{c})$ bytes of storage space, i.e., $O\left(N_\mathrm{s}^{1.5}\right)$ bytes for quasi-planar surfaces and $O\left(N_\mathrm{s}^2\right)$ bytes for general 3D surfaces.

Next, to quantify the performance of TD-AIM for the three surface integral equations in (3.3), the number of spatial FFTs required for solving each one is counted. By computing and storing the spatial FFTs of the propagation matrices $\mathbf{G}_1^{A,\varphi}, \ldots, \mathbf{G}_{N_\mathrm{g}}^{A,\varphi}$ prior to time marching, a total of $2N_\mathrm{g} + 4N_\mathrm{t}$ forward and $4N_\mathrm{t}$ inverse spatial FFTs are computed for the EFIE. Similarly, $3N_\mathrm{g} + 3N_\mathrm{t}$ forward and $3N_\mathrm{t}$ inverse spatial FFTs are required for the MFIE. A straightforward combination for the CFIE would thus require $5N_\mathrm{g} + 4N_\mathrm{t}$ forward and $7N_\mathrm{t}$ inverse spatial FFTs. In our implementation, the number of spatial FFTs required for the CFIE is reduced to $2N_\mathrm{g} + 4N_\mathrm{t}$ forward and $4N_\mathrm{t}$ inverse spatial FFTs using an approach similar to that in [61]. The CFIE cost is reduced by observing that both the EFIE and the MFIE kernels are formulated in terms of the vector potential $\mathbf{A}(\mathbf{r}, t)$, and that each Cartesian component of the temporal derivatives of $\mathbf{A}(\mathbf{r}, t)$ are available on the uniform mesh at the end of Stage (2). Consequently, the MFIE contributions can be obtained from the EFIE computations without any additional FFTs, i.e., space–time samples of $\nabla \times \partial_t \mathbf{A}(\mathbf{r}, t)$ are computed from the space–time samples of $\partial_t^2 \mathbf{A}(\mathbf{r}, t)$ using a higher-order finite difference approach and numerical time integration. (The time integration translates to a trivial complex scalar multiplication in the time-harmonic formulations.) The time integral is evaluated efficiently in the time-marching context by storing the value of the integral at each auxiliary point at the previous time step and adding to it at each time step. Hence, the CFIE computation requires the same number of spatial (and temporal) FFTs as that of the EFIE and a total of $O(N_\mathrm{t} N_\mathrm{c})$ extra operations and $O(N_\mathrm{c})$ extra storage.

A comparison with other time-domain schemes is in order. Irrespective of the nature of the scatterer, the CPU cost and memory requirements of classical MOT solvers scale as $O\left(N_\mathrm{t} N_\mathrm{s}^2\right)$ and $O\left(N_\mathrm{s}^2\right)$, respectively. Therefore, the CPU and memory costs of the TD-AIM scheme always scale better than those of classical solvers, with the exception of the TD-AIM memory cost for 3D surfaces, which scales only on par with that of classical MOT solvers. In [46, 47] algorithms that ignore the temporal Toeplitz structure of (3.5) and employ only spatial FFTs were considered. The computational complexity of those schemes when applied to Stage (2) scales as $O(N_\mathrm{t} N_\mathrm{c} N_\mathrm{g})$, i.e., as $O\left(N_\mathrm{t} N_\mathrm{s}^{1.5}\right)$ for quasi-planar surfaces and as $O\left(N_\mathrm{t} N_\mathrm{s}^2\right)$ for general surfaces (under the above delineated conditions). Therefore, the CPU cost of the present algorithm always scales better than time-domain schemes that use only spatial FFTs. The memory requirements of those schemes, however, are of the same order as those of the present algorithm. Finally, the CPU and memory requirements of general purpose, multilevel PWTD schemes scale as $O\left(N_\mathrm{t} N_\mathrm{s} \log^2 N_\mathrm{s}\right)$ and $O(N_\mathrm{g} N_\mathrm{s})$, respectively [16]. Therefore, when compared to multilevel PWTD acceleration, the TD-AIM asymptotically scales worse for general 3D surfaces and has the same computational cost for quasi-planar structures. Nonetheless, in our experience, TD-AIM remains competitive with multilevel PWTD for 3D surfaces up to tens of thousands of spatial unknowns, and generally outperforms it for quasi-planar structures.

3.3.5 Parallelization

The practical bottleneck of the TD-AIM is its memory requirements. Compared to its frequency-domain counterpart, the TD-AIM requires $O(N_\mathrm{g})$ times more memory because it needs to store the temporal history of sources to compute retarded fields throughout the auxiliary mesh. To moderate the impact of this memory bottleneck, this section presents a TD-AIM parallelization strategy targeting distributed memory computers that communicate via message passing. While the TD-AIM scheme's memory apetite serves as the main motivation behind the parallelization effort, parallel efficiency is not ignored and load balancing and scalability issues are also addressed.

The following approach to parallelization is based on the balanced distribution of the uniform grid and the FFT operations related to it among the P available processors. Because zero-padding (doubling) is required to multiply a (block-)Toeplitz matrix via FFTs, all 4D FFTs are done on arrays of size *at most* $2N_{cx} \times 2N_{cy} \times 2N_{cz} \times 2N_\mathrm{g}$ (the temporal array size varies from time step to time step), which are either derived from the blocked aggregates in $\mathbf{G}^{\mathbf{H},A,\varphi}$ or are the zero-padded currents and fields on the auxiliary grid. To reduce the memory demand per processor, the arrays are distributed among the processors by one-dimensional (1D) slab-decomposition: each processor stores $2N_{cx}/P \times 2N_{cy} \times 2N_{cz} = 8N_\mathrm{c}/P$ spatial entries over time as depicted in Fig. 3.2. Because now only part of the auxiliary grid is available to each

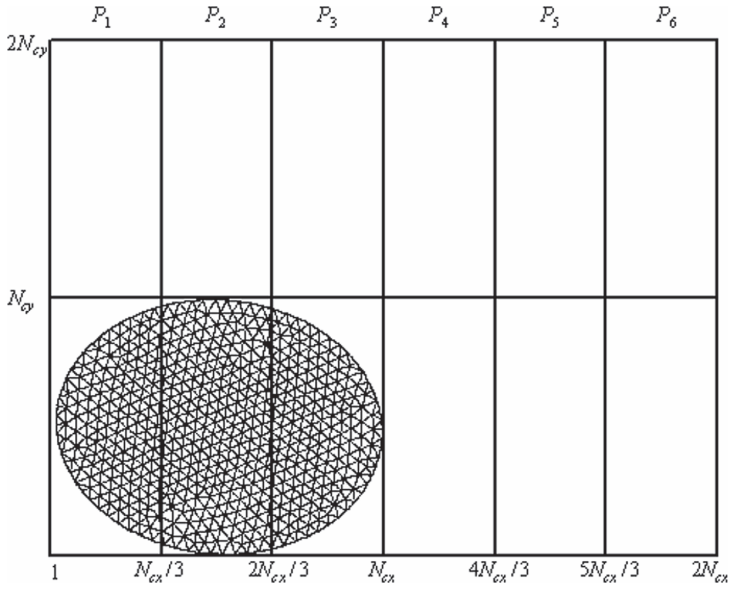

Fig. 3.2. One-dimensional slab-decomposition for $P = 6$. The auxiliary mesh is of size $N_{cx} \times N_{cy} \times N_{cz}$ (z dimension is not shown) and is distributed by dividing the x dimension into slabs. Due to doubling, each processor stores $N_{cx}/3 \times 2N_{cy} \times 2N_{cz}$ spatial entries over time

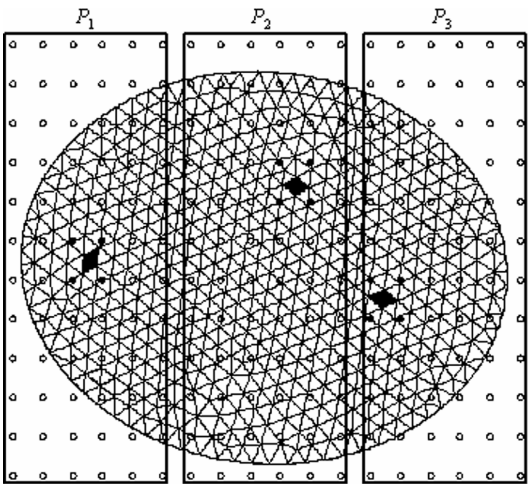

Fig. 3.3. Stage (1) of the algorithm: parallel projection onto the uniform mesh. Here, $P = 6$, $N_{cx} = 18$, and $N_{cy} = 12$ (z dimension is not shown). Only the part of the uniform mesh that is projected to by the active processors is shown. Three RWG functions and the related nodes are highlighted. Each processor projects all the RWG functions that affect its section of the mesh

processor, all four stages of the algorithm should be modified accordingly as illustrated in Figs. 3.3 and 3.4 and described below.

1. At time step l, each processor projects the current density $\mathbf{I}_{l-1}$ onto its section of the auxiliary grid (Fig. 3.3). Because approximately half of the processors do the projection and because the primary mesh is not uniform, the distribution of this effort among processors is unbalanced. Nonetheless, this does not significantly affect the parallel efficiency because of the minute amount of CPU resources required to compute local projections as compared to FFTs.
2. The space–time FFTs are computed in parallel using the FFTW library [64]. Specifically, each processor computes two-dimensional (2D) FFTs in the y and z dimensions of its section of the zero-padded current-arrays (Fig. 3.4a). Next, all arrays are transposed, which requires an all-to-all processor communication. Finally, each processor computes FFTs in the x dimension to complete the spatial FFTs [44, 52, 64] (Fig. 3.4b). Hence, the auxiliary current coefficients at time $(l-1)\,\Delta t$ is transformed to the spectral domain ($k$space). These spectral-domain arrays are stored to minimize repeated computations and communication. Then, the processors concurrently compute temporal FFTs at each of their $8N_c/P$ spatial nodes according to the blocking scheme of Sect. 3.3.3 to transform the current to the spectral-frequency domain (Fig. 3.4c). Next, each processor multiplies its part of the transformed currents and block aggregates to obtain a part of fields in the spectral-frequency domain. Once these

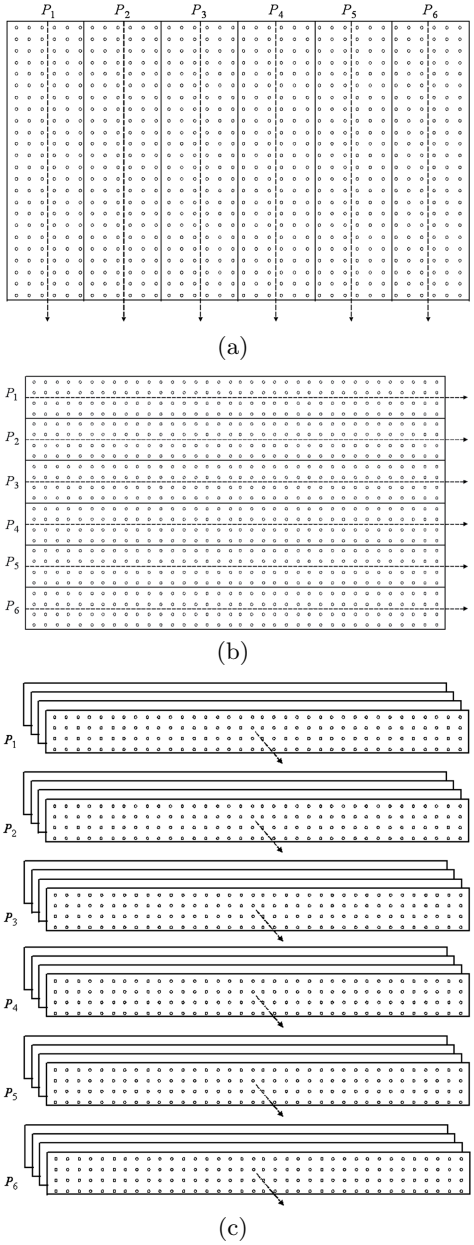

Fig. 3.4. Stage (2) of the algorithm: parallel space–time FFTs. Here, $P = 6$, $N_{cx} = 18$, and $N_{cy} = 12$ (z dimension is not shown). (**a**) Each processor computes six FFTs of size 24 in the y dimension. This is followed by an all-to-all communication step that transposes the arrays. (**b**) Each processor then computes four FFTs of size 36 in the x dimension for the transposed arrays. (**c**) Temporal FFTs, the size of which depends on the time step, are computed. Here, each processor computes 144 FFTs of size 4

fields are found, the above steps are reversed: Each processor computes inverse temporal FFTs to find temporal chunks of future fields in the spectral domain ($k$space), and these *partial* future fields are added to those obtained from previous time steps at each one of the $8N_c/P$ spatial points. Finally, the inverse spatial FFTs of the fields *only* at the next time step are computed to obtain the *complete* field in the space–time domain at time $l\Delta t$. As described here, the computational cost of Stage (2) is $O\left(N_t N_c \left(\log N_c + \log^2 N_g\right)/P\right)$ and its per-processor memory requirement is $O\left(N_g N_c/P\right)$. Because there are only two global communications for transposing the arrays at each time step, the total communication cost is $O\left(N_t N_c\right)$. The work in this stage is equally distributed if N_{cx}/P and N_{cy}/P are integers.

3. Similar to Stage (1), each processor interpolates the fields on its section of the auxiliary grid to the surface mesh, that is, the processors consider all the unknowns on the primary mesh that are affected by their sections of the arrays.
4. The near-field interactions are corrected in parallel. Let aN_s denote the number of nonzero elements of the $\mathbf{Z}_{l-l'}^{\text{near}}$ matrices, i.e., the number of near-field corrections. To multiply the $\mathbf{Z}_{l-l'}^{\text{near}}$ matrices in parallel, the nonzero elements are distributed among the processors using a column-based decomposition, i.e., each processor stores and multiplies approximately aN_s/P matrix elements plus or minus one column of the matrices. Hence, each processor stores a short history (l^{near} time steps) of parts of the primary currents that correspond to its columns of $\mathbf{Z}_{l-l'}^{\text{near}}$.

Once all four stages of the TD-AIM algorithm are completed at a given time step l and $\mathbf{V}_l^{\text{scat}}$ is formed, (3.5) is solved in parallel for the current density at the next time step. Because $\mathbf{Z}_0$ matrix in general has $O\left(N_s\right)$ nonzero elements, the communication cost dominates the parallel solution time, which does not exhibit good scalability, and hampers the overall parallel efficiency [65]. The solution time becomes sub-dominant, however, as the problem becomes electrically large, i.e., as N_s, N_c, and N_g increase.

3.3.6 Accuracy and Computational Complexity Verification

This section presents numerical examples that demonstrate the operation of the TD-AIM accelerated MOT-TDIE solver. First, two matching approaches are compared. Then, the computational complexity, memory requirements, and parallel efficiency of the accelerated solver are examined by simulating two types of scatterers that represent the best- and worst-case scenarios for the algorithm, viz. plates and spheres. In all simulations, the temporal basis functions are fourth-order Lagrange interpolants [7], and the MFIE contributions, when needed, are computed using the numerical scheme presented in Sect. 3.3.4, with a fifth-order accurate temporal integration and a fourth-order accurate central differencing scheme. All the results in this section were obtained on cluster of 1-GHz Pentium III processors with 1 GB of memory.

Matching Accuracy

To investigate the accuracy of the moment- and field-matching approaches, the interaction between two RWG functions is computed and the error incurred by the TD-AIM is examined. A flat RWG basis function $\mathbf{S}_{k'}(\mathbf{r})$ that is anchored at the origin supports an impressed current $\mathbf{S}_{k'}(\mathbf{r})\,\mathrm{e}^{-2(\pi f_{\max} t-12)^2/9}$, where $f_{\max}$ quantifies the maximum frequency of interest and more than 99.997% of the Gaussian pulse's power is at frequencies below $f_{\max}$. The fields radiated by this basis function are measured on another flat RWG function $\mathbf{S}_k(\mathbf{r})$ (Fig. 3.5). The auxiliary grid is centered at $x = 0.5\Delta s_x$, $y = 0.5\Delta s_y$, and $z = 0.5\Delta s_z$, where Δs_x, Δs_y, and Δs_z are the grid spacings. The relative energy error in the tested fields is defined as

$$\Delta^{\mathrm{AIM}} = \left[\sum_{l=1}^{N_{\mathrm{t}}} \left(\mathbf{V}_l^{\mathrm{scat}}(k) - \mathbf{V}_l^{\mathrm{scat,AIM}}(k)\right)^2 \Big/ \sum_{l=1}^{N_{\mathrm{t}}} \left(\mathbf{V}_l^{\mathrm{scat}}(k)\right)^2\right]^{0.5}, \quad (3.15)$$

where $\mathbf{V}_l^{\mathrm{scat}}$ is given in (3.5) and

$$\mathbf{V}_l^{\mathrm{scat,AIM}} = \sum_{l'=\max(1,l-N_{\mathrm{g}})}^{l-1} \mathbf{Z}_{l-l'}^{\mathrm{FFT}}(k,k')\,\mathbf{I}_{l'}(k'). \quad (3.16)$$

Figures 3.6 and 3.7 present Δ^{AIM} as a function of the center-to-center distance between $\mathbf{S}_{k'}(\mathbf{r})$ and $\mathbf{S}_k(\mathbf{r})$. For the results presented in both figures, $f_{\max} = c$ ($\lambda_{\min} = c/f_{\max} = 1\,\mathrm{m}$), $\Delta t = 1/(30c)$ ($\beta = 1/15$), in order to capture the significant part of the pulse for even the farthest interaction, $N_{\mathrm{t}} = 250$, and the number of dipoles is 8 and 64. In Fig. 3.6, $\Delta s_x = \Delta s_y = \Delta s_z = \lambda_{\min}/20 = 5\,\mathrm{cm}$ while in Fig. 3.7, $\Delta s_x = \Delta s_y = \Delta s_z = \lambda_{\min}/40 = 2.5\,\mathrm{cm}$. In both figures, the time-basis functions are approximate prolate functions [9, 10] that exhibit excellent time- and band-limitedness properties allowing accurate evaluations of the integrals in (3.6c). In the field-matching approach these functions are also used to interpolate the samples of the time signatures. In Figs. 3.6b and 3.7b, the near-field sphere on which the fields are matched is chosen to be at 50 cm. Taken as a whole, Figs. 3.6 and 3.7 show that the error made by (3.7) for both moment- and field-matching approaches decreases as the auxiliary-grid

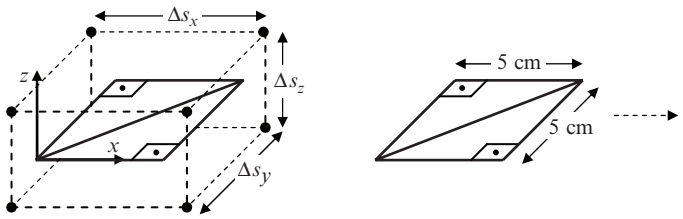

Fig. 3.5. The RWG functions and some of the auxiliary points used

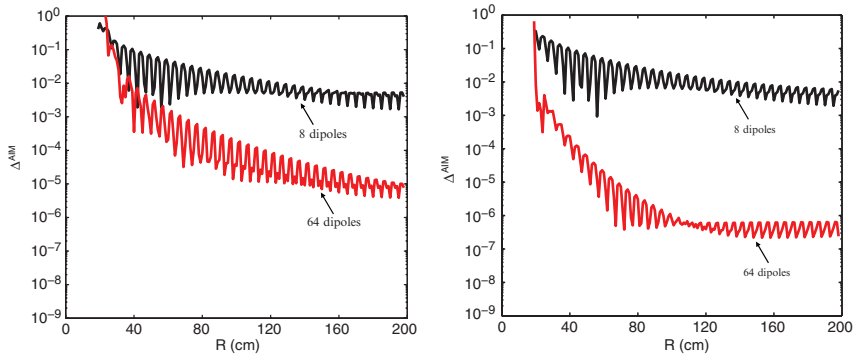

Fig. 3.6. Relative energy error Δ^{AIM} for the RWG functions in Fig. 3.5 as a function of their center-to-center distance for $\Delta s_x = \Delta s_y = \Delta s_z = \lambda_{\min}/20 = 5\,\mathrm{cm}$. (**a**) The multipole moments are matched from zero up to order one (8 dipoles) and up to order three (using 64 dipoles). (**b**) The fields are matched on a near-field sphere at 50 cm using 8 and 64 dipoles

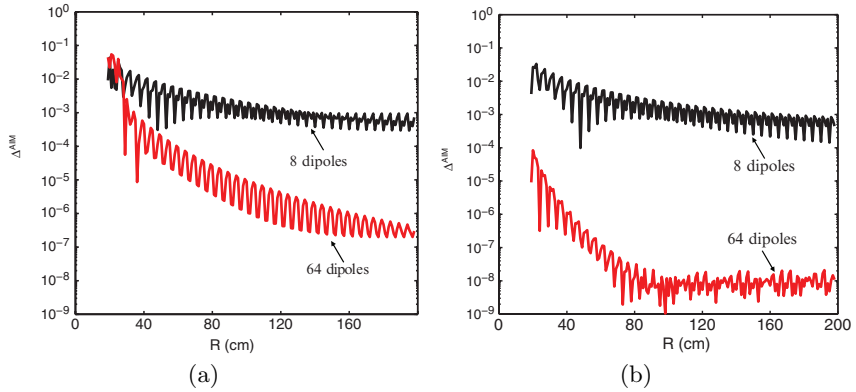

Fig. 3.7. Relative energy error Δ^{AIM} for the RWG functions in Fig. 3.5 as a function of their center-to-center distance for $\Delta s_x = \Delta s_y = \Delta s_z = \lambda_{\min}/40 = 2.5\,\mathrm{cm}$. (**a**) The multipole moments are matched from zero up to order one (using 8 dipoles) and up to order three (using 64 dipoles). (**b**) The fields are matched on a near-field sphere at 50 cm using 8 and 64 dipoles

spacing becomes smaller. These figures also show that the moment-matching approach produces results accurate enough for practical applications. Even though field-matching results in more accurate matrix elements, because of the reasons detailed in Sect. 3.3.2, moment-matching is utilized in the hybrid solver for simulations presented in Sect. 3.4. A more detailed error analysis of moment-matching approach for time-domain surface integral equations (including CFIE) can be found in [17].

Computational Complexity Verification

The theoretical computational complexity, memory requirements, and parallel efficiency of the TD-AIM were derived in Sects. 3.3.4 and 3.3.5. Here, the scheme's practical efficiency is evaluated by analyzing scattering plates and spheres. In what follows, all scatterers are centered at the origin of the coordinate system, and plate side-lengths and sphere diameters are denoted L_p and L_s, respectively. Scattering from square plates is analyzed using the EFIE, whereas scattering from spheres is analyzed using the CFIE ($\alpha = 0.4$). The TD-AIM parameters are chosen to minimize the CPU time and memory product while ensuring that a relative root-mean-square RCS error with respect to a frequency-domain method-of-moments (MOM) solver, which uses the same mesh as the TD-AIM accelerated MOT-TDIE solver, is less than 0.01.

Figure 3.8a,b plot the average TD-AIM wall-clock time per time step (i.e., the total wall-clock time spent to construct $\mathbf{V}_l^{\mathrm{scat}}$ divided by N_t). Figure 3.9a,b plot the corresponding *measured* peak memory requirement of the algorithm which also includes operating system overhead. The figures show the parallel efficiency of the algorithm as the surface areas of the plates and spheres are increased 625 and 144 times, respectively, i.e., L_p varies from 1 to 25 m and L_s varies from 1 to 12 m. Both the CPU time and the memory requirements of the algorithm exhibit good parallel efficiency as the size of the scatterers increase. The computational complexity of TD-AIM with respect to the number of surface unknowns N_s is verified in Fig. 3.10a,b using the data points in Fig. 3.10a,b: The total CPU time per time step and the memory requirements of TD-AIM are computed by multiplying the data points in Fig. 3.10a,b with the corresponding number of processors P. Thus, if the implementation had ideal parallel efficiency all the data points for a given N_s would coincide in Fig. 3.10. The computational complexity of the implementation is in good

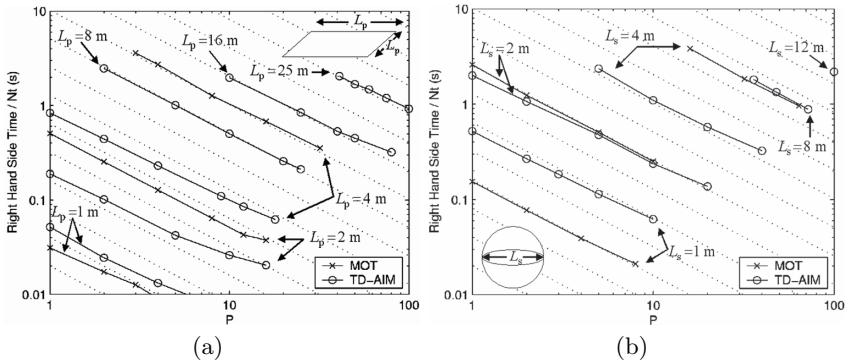

Fig. 3.8. Average wall-clock time to compute $\mathbf{V}_l^{\mathrm{scat}}$ at each time step for (**a**) plates and (**b**) spheres. *Dashed lines* are ideal speed-up tangents

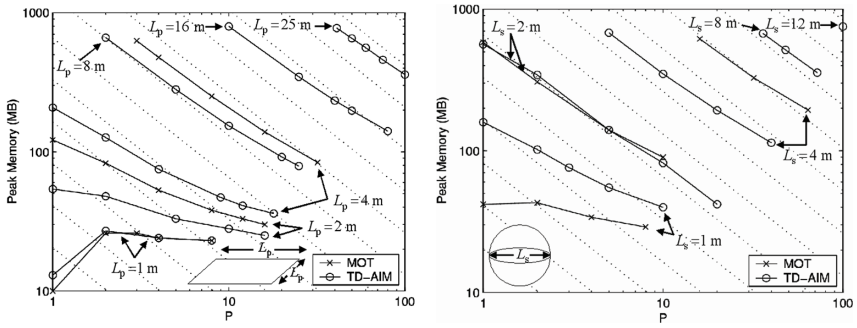

Fig. 3.9. Observed peak storage requirement among all processors for (**a**) plates and (**b**) spheres. *Dashed lines* are ideal speed-up tangents

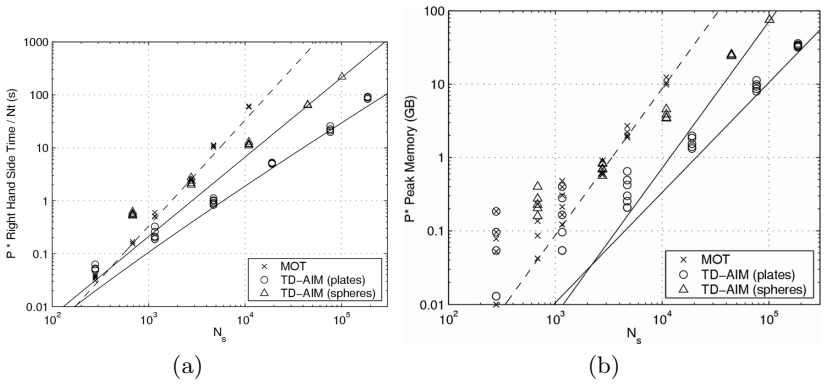

Fig. 3.10. TD-AIM versus MOT for plates and spheres. (**a**) Computational complexity. The lines are parallel to N_s^2, $N_s^{1.5}$, and $N_s \log^2 N_s$. (**b**) Memory requirement. The lines are parallel to N_s^2, N_s^2, and $N_s^{1.5}$

agreement with the trends predicted in Sect. 3.3. Figure 3.10a,b also compare the computational demands of TD-AIM with those of a classical (parallel) MOT scheme: The TD-AIM accelerated MOT-TDIE solver outperforms the classical one for as little as $N_s \approx 500$ for plate and $N_s \approx 2,500$ for sphere simulations.

3.4 Hybridization and Applications to Challenging EMI Problems

Even though the TD-AIM accelerator renders stand-alone MOT-TDIE field solvers useful for analyzing transient fields on electrically large and multi-scale platforms, these solvers are of little use when these platforms carry

cable-interconnected subwavelength scale, and potentially nonlinear electronic subsystems. To characterize field interactions with such structures, the hybridization of MOT-TDIE field solvers with specialized subsystem simulators is called for. For example, to facilitate the efficient analysis of real-world EMI problems, MOT-TDIE field solvers should be hybridized with a circuit solver that computes node voltages and branch currents in nonlinear lumped-element circuits, a cable solver that computes voltages and currents along multiconductor transmission lines, and modules that facilitate the macromodel description of electronic subsystems.

This section elucidates the hybridization of MOT-TDIE field solvers with subsystem modelers and demonstrates the versatility of the resulting hybrid simulator through its application to real-world EMI problems.

3.4.1 Hybridization with Circuit Solvers

It is well-known that electrically small components can be effectively and accurately modeled as (nonlinear) lumped-element circuits using modified nodal analysis (MNA)-SPICE solvers [66–68]. MNA enforces Kirchhoff's equations on non-ground nodes and solves the resulting nonlinear system of equations for non-ground node voltages and voltage source currents.

Recently, TDIE-field solvers were hybridized with MNA-circuit solvers and applied to the analysis of transient field interactions with electrically large platforms loaded with nonlinear lumped-element circuits [26, 27]. Hybridization of field and circuit solvers (i.e., combining the MOT and MNA systems) results in a coupled nonlinear system of equations that is solved simultaneously for all field and circuit solver unknowns via Newton–Raphson. The parallel scalability of the hybrid simulator is maintained by distributing the field and circuit solvers' computational work to two separate groups of processors [27]. This simple but effective parallization strategy results in near-ideal scalability since these groups of processors communicate only during the iterative solution of the coupled system. Additionally, this separation strategy allows for the separate development and optimization of field and circuit solvers.

3.4.2 Hybridization with Cable Solvers

Under transverse electromagnetic (TEM)-like propagation assumption, fields along multiconductor transmission lines are represented by voltage and current waves satisfying the well-known transmission-line equations [69, 70]. A 1D TDIE is obtained by enforcing the boundary conditions relating voltages and currents at the transmission-line terminations. The standard MOT recipe, which originally was developed for solving 3D TDIEs pertinent to scattering problems, is used to solve the 1D TDIEs describing transmission-line signal propagation. The lossy and dispersive nature of the guided-wave propagation along the transmission line is accounted for by using the pertinent Green function. The TDIE-cable solver's computational bottleneck is the evaluation

of excitation voltages and currents, which requires the convolution of Green functions with the "past" voltages and currents. The computational complexity of this operation, which scales as $O\left(N_{\mathrm{t}}^2\right)$, is reduced to $O\left(N_{\mathrm{t}} \log^2 N_{\mathrm{t}}\right)$ using the FFT acceleration algorithm of [53]. The main advantage of this acceleration scheme is that it applies regardless of the method used for obtaining the Green function (measurements, direct time-domain computation, Fourier transformation of frequency-domain models).

The TDIE-field solver was hybridized with TDIE-cable and MNA-circuit solvers and applied to the EMI analysis of electrically large, real-world problems involving coaxial and unshielded multiconductor cables [25, 30]. Connectors and loads that terminate the cables are assumed to be electrically small and modeled with lumped element circuit networks; node voltages and branch currents on these circuits are computed using the circuit solver. The hybrid simulator solves the coupled system of equations, which is obtained by combining the two MOT and the MNA systems, simultaneously for all field, cable, and circuit unknowns. The same parallization strategy is followed; the cable solver's computational work is assigned to the circuit solver's group of processors.

3.4.3 Incorporation of Macromodelers

Macromodels are reduced multiport transfer function representations of electronic subsystems that would require large circuit networks if modeled using lumped elements [71, 72]. They have long been employed in circuit solvers to reduce computational costs and avoid loss of accuracy in system-level analysis. Gains in CPU time and memory are attained by using recursive convolution algorithms and reduced-order model generation techniques [73–77].

In practice, macromodels can be connected to ports of subsystems modeled either by the circuit- or field-solver component of the hybrid simulator; hence, they need to be interfaced with both solvers simultaneously. However, the integration of the commonly used admittance parameter macromodels – or any other macromodel defined by a single set of network parameters – with each solver requires a separate treatment, because the field-solver unknowns are current quantities, while the circuit-solver unknowns are voltage quantities. The effective incorporation of the macromodels with fast hybrid simulators requires the identification of associated computational bottlenecks in the solution of the resulting coupled system of equations and the use of fast recursive convolution schemes to overcome these bottlenecks [32].

3.4.4 Applications

In the applications presented below, all the structures are excited by plane waves and/or "delta-gap" voltage sources. Electric fields $\mathbf{E}^{\mathrm{inc}}(\mathbf{r}, t)$ of $\hat{\mathbf{p}}$-polarized plane waves propagating in the $\hat{\mathbf{k}}$ direction and voltages $V^{\mathrm{inc}}(t)$ of localized sources are expressed as

$$\mathbf{E}^{\mathrm{inc}}(\mathbf{r},t)=\hat{\mathbf{p}}E_0G_{\mathrm{mod}}\left(t-\mathbf{r}\cdot\hat{\mathbf{k}}/c\right), \tag{3.17a}$$

$$V^{\mathrm{inc}}(t)=V_0G_{\mathrm{mod}}(t), \tag{3.17b}$$

where E_0 and V_0 are the electric field peak and voltage amplitudes, and $G_{\mathrm{mod}}(t)=\mathrm{e}^{-(t-t_{\mathrm{p}})^2/2\sigma^2}\cos\left(2\pi f_{\mathrm{c}}(t-t_{\mathrm{p}})\right)$ is a modulated Gaussian signature function with modulation frequency f_{c}, delay $t_{\mathrm{p}}=8\sigma$, duration $\sigma=3/(2\pi f_{\mathrm{bw}})$, and bandwidth f_{bw}. This choice of parameters guarantees that more than 99.997% of $G_{\mathrm{mod}}(t)$'s power resides inside the frequency band $[f_{\mathrm{min}}=f_{\mathrm{c}}-f_{\mathrm{bw}},f_{\mathrm{max}}=f_{\mathrm{c}}+f_{\mathrm{bw}}]$. All simulations were carried on a cluster of 2-GHz Apple G5 processors.

Monopole Antennas Mounted on a Car

The hybrid simulator is used in the EMI analysis of three antennas mounted on a 1984 Chevrolet Camaro Z28 (Fig. 3.11a): Two 10 cm long monopole antennas M_1 and M_2 and one 50 cm long monopole antenna M_3 are mounted on the mirrors and near the rear of the car, respectively (Fig. 3.11b). Antennas M_1 and M_2 are connected to voltage sources using 15 cm long cables T_1 and T_2, and antenna M_3 is connected to a 50-Ω load located inside an electronic shielding box in the trunk using a 1.20 m long cable T_3 (Fig. 3.11b). Cables T_1, T_2, and T_3 are RG-58 coaxial cables with foam polyethylene dielectric filling, outer shield radius $a_{\mathrm{o}}=0.1524$ cm, inner shield radius $a_{\mathrm{i}}=0.1397$ cm, and wave speed $c_{\mathrm{CBL}}=0.78c$. Cables T_1 and T_2 are embedded within the mirror cavities; hence, they only interact with external fields via their terminations. Cable T_3 interacts with external fields along its shield as well as via its terminations. Cable T_3's shield transfer impedance is given by $\hat{T}^{\mathrm{i}}(f)=R_0\left[(1+j)(a_{\mathrm{o}}-a_{\mathrm{i}})/\delta\right]/\sinh\left[(1+j)(a_{\mathrm{o}}-a_{\mathrm{i}})/\delta\right]+j2\pi fL_{\mathrm{a}}$, where $\delta=\sqrt{1/(\pi f\sigma\mu)}$ is the skin depth, $\sigma=5.0\times10^7\ \mathrm{S\,m^{-1}}$ is the conductivity, $\mu=\mu_0$ is the permeability, $R_0=14.3\,\mathrm{m\Omega\,m^{-1}}$, and $L_a=1.0\,\mathrm{nH\,m^{-1}}$ [78]. The two voltage sources connected to cables T_1 and T_2 have $V_0=1$ V, $f_{\mathrm{min}}=0.4$ GHz, $f_{\mathrm{c}}=0.8$ GHz, and $f_{\mathrm{max}}=1.2$ GHz. The simulation is carried out for $N_{\mathrm{t}}=2,000$ time steps with $\Delta t=55$ ps. The current density on the surfaces modeling the car, the electronic shielding box, the exposed cable T_3 and the voltages on the cable loads are modeled by 128 976 surface, 667 wire, 44 junction basis functions and 6 circuit unknowns, respectively. The number of cable unknowns is six. Coupling of the external and guided fields is realized at 55 points. The temporal basis functions used for discretizing the 3D and 1D TDIEs are prolate-based band-limited interpolant with $8\Delta t$ half-width [9, 10], and third-order Lagrange polynomial [7], respectively. The TD-AIM kernel matches up to third-order moments, $\gamma=6$, $\Delta s_x=40.84$ cm, $\Delta s_y=40.84$ cm, and $\Delta s_z=53.37$ cm; this choice of TD-AIM parameters results in $N_{\mathrm{c}}=192\times81\times35$ auxiliary grid points. Figure 3.12 presents the transient coupled voltages observed at node 1 (Fig. 3.11b) due to radiation

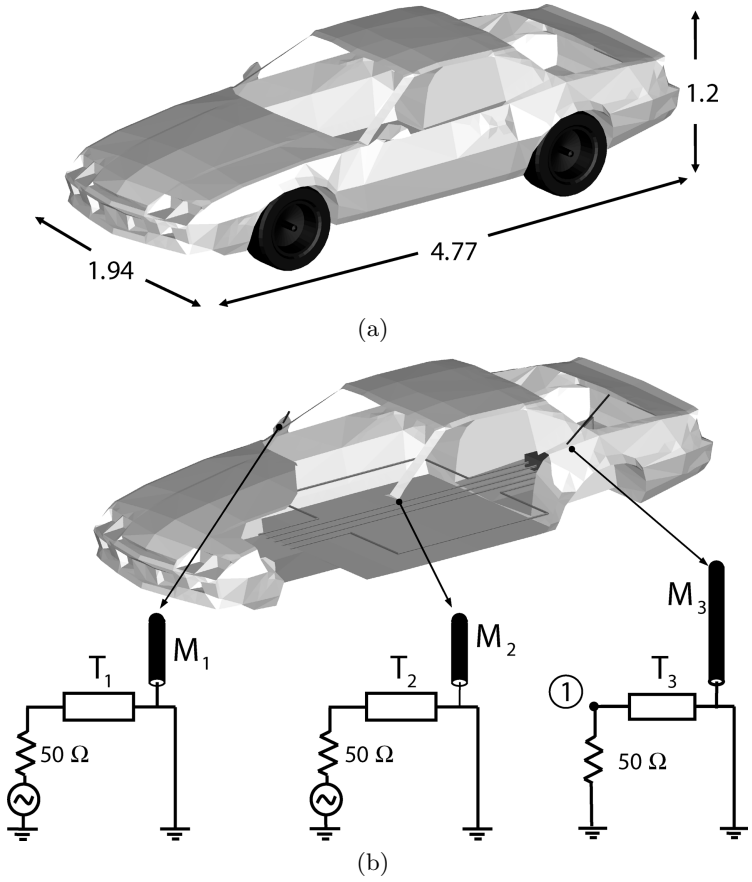

Fig. 3.11. Monopole antennas mounted on a car. (**a**) Dimensions of the car. (All dimensions are in meters.) (**b**) Locations of the monopole antennas and descriptions of their feed networks

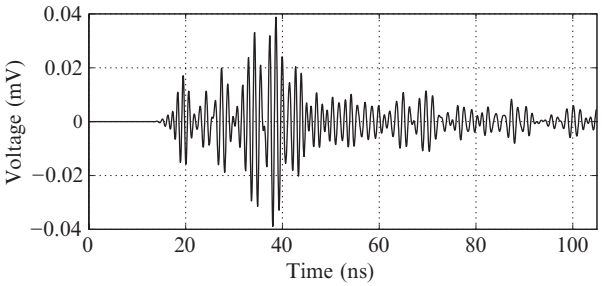

Fig. 3.12. Transient voltage observed at node 1 (Fig. 3.11b) due to external fields radiated by the short monopole antennas

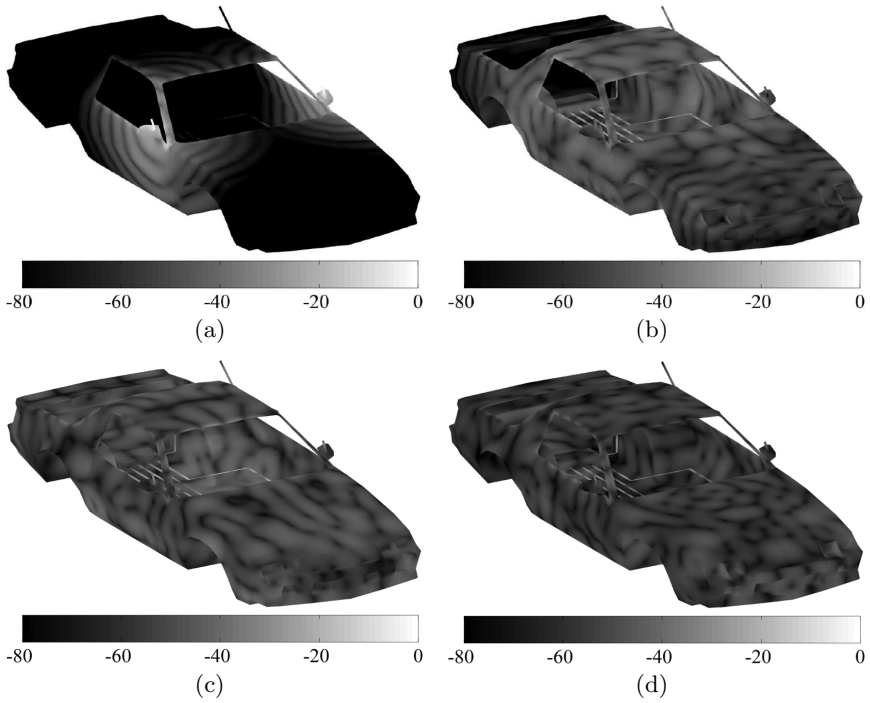

Fig. 3.13. Snapshots of the transient currents on the surfaces modeling the car, the antennas, and the exposed coaxial cable (in dB scale) at (**a**) $\Delta t = 6.6\,\text{ns}$, (**b**) $\Delta t = 9.9\,\text{ns}$, (**c**) $\Delta t = 13.2\,\text{ns}$, and (**d**) $\Delta t = 26.4\,\text{ns}$

from monopoles M_1 and M_2. Figure 3.13a–d present snapshots of the current density on the surfaces modeling the car, the antennas, and the exposed coaxial cable at different time instances. The hybrid simulator required 120 GB of memory and 40 m to fill the matrices and 1.46 h to find the solution using 121 processors (120 for the field solver, 1 for the circuit and cable solvers).

PC Enclosures in a Cockpit

The hybrid simulator is used in the EMI analysis of three RG-58 coaxial cables connecting three PCs located inside an airplane cockpit. All of the PCs have identical outer dimensions and two of them, which are close to the floor of the cockpit, contain a mother board and two daughter cards (Fig. 3.14a,b). The two daughter cards are identical in size; the daughter card, which is closer to the back of the cockpit (first card), is connected to the mother board via eight pins, and the other one (second card) is connected via one pin (see [79] for detailed description of the card configuration). One coaxial cable T_1 connects the feed points (pins) of the second card in the two PCs. Two cables T_2 and T_3 connect the two PCs on the right and are terminated with 75-Ω

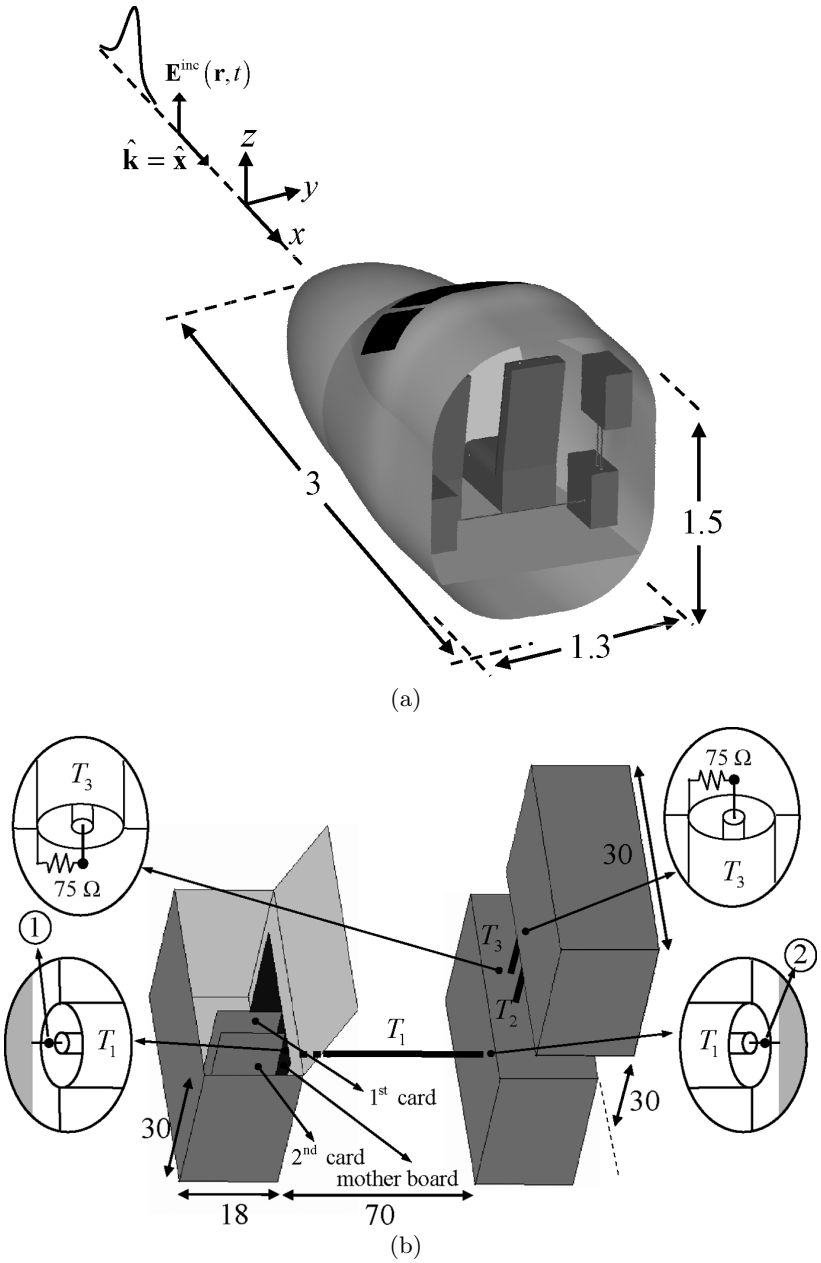

Fig. 3.14. PCs located in a cockpit. (**a**) Dimensions of the cockpit and the external plane wave excitation. (All dimensions are in meters.) Although not shown in the figure, the back of the cockpit is closed during the simulations. (**b**) Dimensions of the PC boxes (all have identical sizes) and the coaxial cables. (All dimensions are in centimeters.)

resistors (Fig. 3.14b). The lengths of cables T_1, T_2, and T_3 are 74, 30, and 30 cm, respectively. Surfaces modeling the floor and the seats, the surface separating the nose cavity from the rest of the cockpit, the surface at the back of the cockpit, and the surfaces modeling the daughter cards inside the PCs are assumed resistive with 377-Ω impedance. The structure is illuminated by a plane wave incident on the cockpit nose with $E_0 = 3,000\ \mathrm{V\,m^{-1}}$, $\hat{\mathbf{k}} = \hat{\mathbf{x}}$, $\hat{\mathbf{p}} = \hat{\mathbf{z}}$, $f_{\min} = 0.9$ GHz, $f_{\mathrm{c}} = 1.7$ GHz, and $f_{\max} = 2.5$ GHz (Fig. 3.14a). The simulation is carried out for $N_{\mathrm{t}} = 1,600$ time steps with $\Delta t = 33$ ps. The current density on the surfaces modeling the cockpit, the PCs , the card configurations and the voltages on the cable loads are modeled by 284 179 surface, 152 wire, 136 junction basis functions and 6 circuit unknowns, respectively. The number of cable unknowns is six. Coupling of the external and guided fields is realized at 158 points. The temporal basis functions used for discretizing the 3D and 1D TDIEs are prolate-based band-limited interpolant with $8\Delta t$ half-width [9, 10] and third-order Lagrange polynomial [7], respectively. The TD-AIM kernel matches up to third-order moments, $\gamma = 5$, $\Delta s_x = 15.43$ mm, $\Delta s_y = 15.93$ mm, and $\Delta s_z = 15.93$ mm; this choice of TD-AIM parameters results in $N_{\mathrm{c}} = 200 \times 100 \times 90$ auxiliary grid points. Figure 3.15a,b present the transient coupled voltages observed at nodes 1 and 2 (Fig. 3.14b) due to the plane wave excitation and Fig. 3.16a,b show that

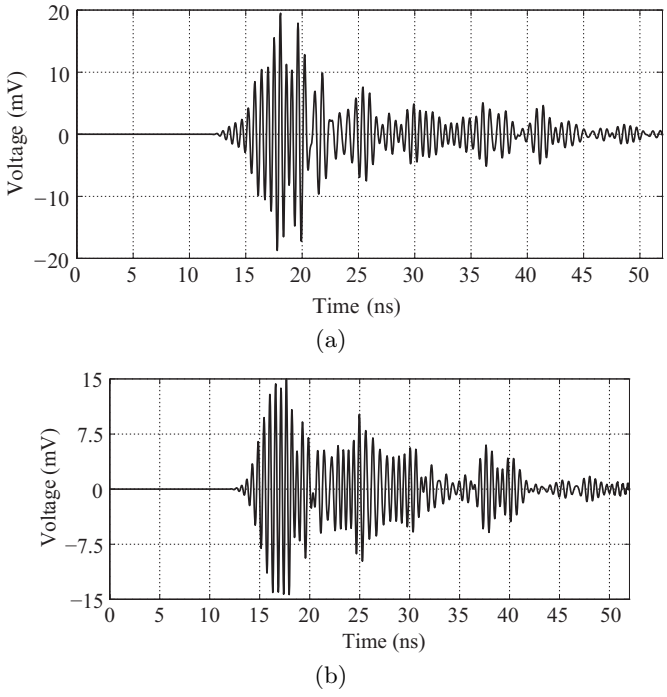

Fig. 3.15. Transient voltages observed at nodes (**a**) 1 and (**b**) 2 due to plane wave excitation

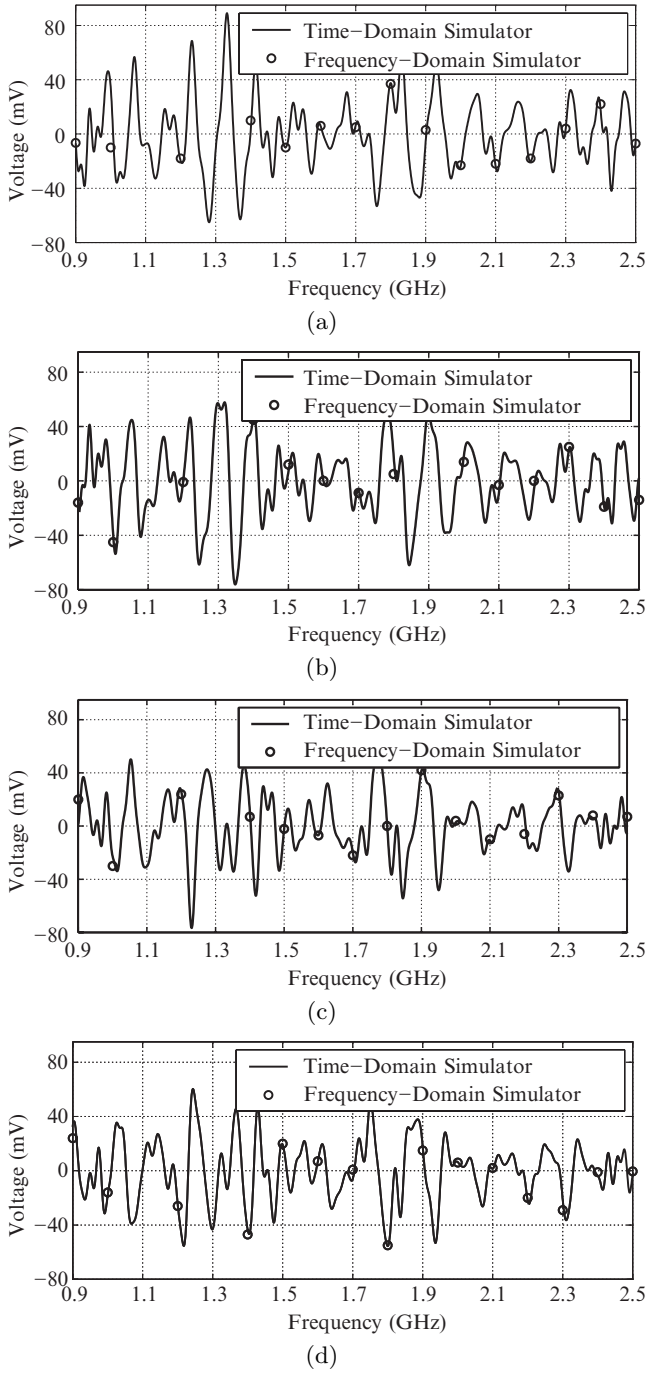

Fig. 3.16. Frequency-domain voltages observed at nodes 1 and 2: (**a**) real and (**b**) imaginary parts of voltage at node 1; (**c**) real and (**d**) imaginary parts of the voltage at node 2

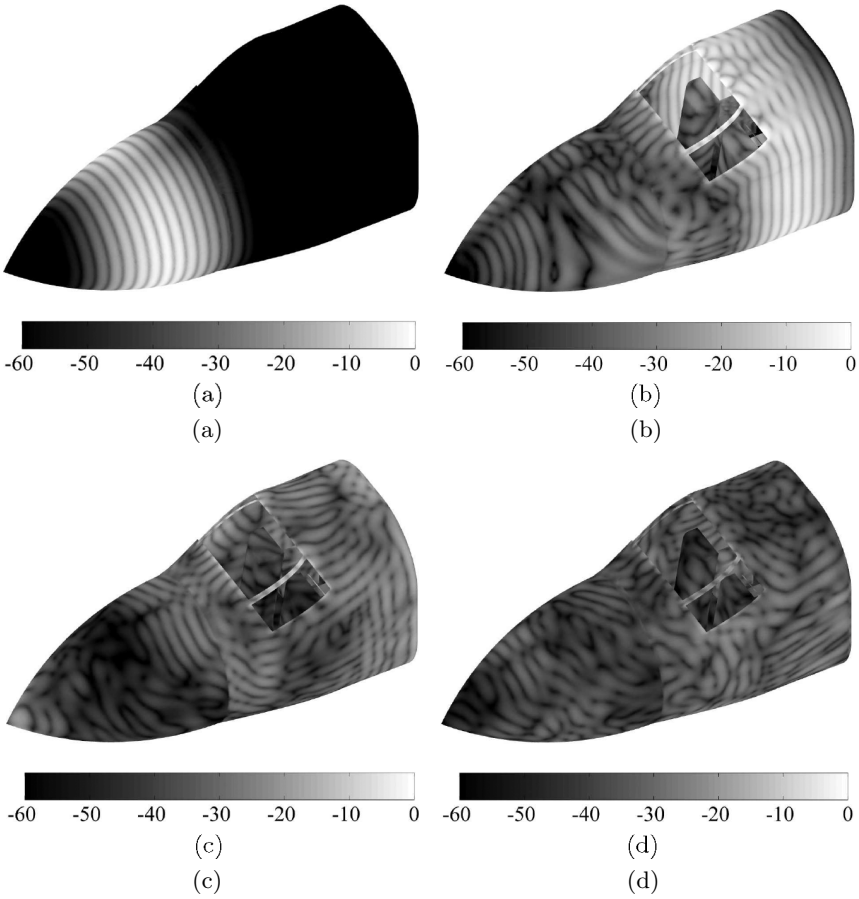

Fig. 3.17. Snapshots of the transient currents on the surfaces modeling the cockpit, the PCs, the card configurations, and the coaxial cables (in dB scale) at (**a**) $\Delta t = 8.25\,\text{ns}$, (**b**) $\Delta t = 13.2\,\text{ns}$, (**c**) $\Delta t = 15.675\,\text{ns}$, and (**d**) $\Delta t = 18.15\,\text{ns}$

frequency-domain voltages observed at these obtained by the hybrid simulator agree well with those obtained by a similar frequency-domain simulator. Figure 3.17a–d presents snapshots of the current density on the surfaces modeling the cockpit, the PCs, the card configurations, and the coaxial cables at different time instances. The hybrid simulator required 310 GB of memory and 31 m to fill the matrices and 2.14 h to find the solution using 201 processors (200 for the field solver, 1 for the circuit and cable solvers).

RG-58 and UTP-CAT5 Cables Located on an Aircraft

The hybrid simulator is used in the EMI analysis of RG-58 and UTP-CAT5 cables located on a Beechcraft King Air 250 aircraft (Fig. 3.18a). A 1 m long

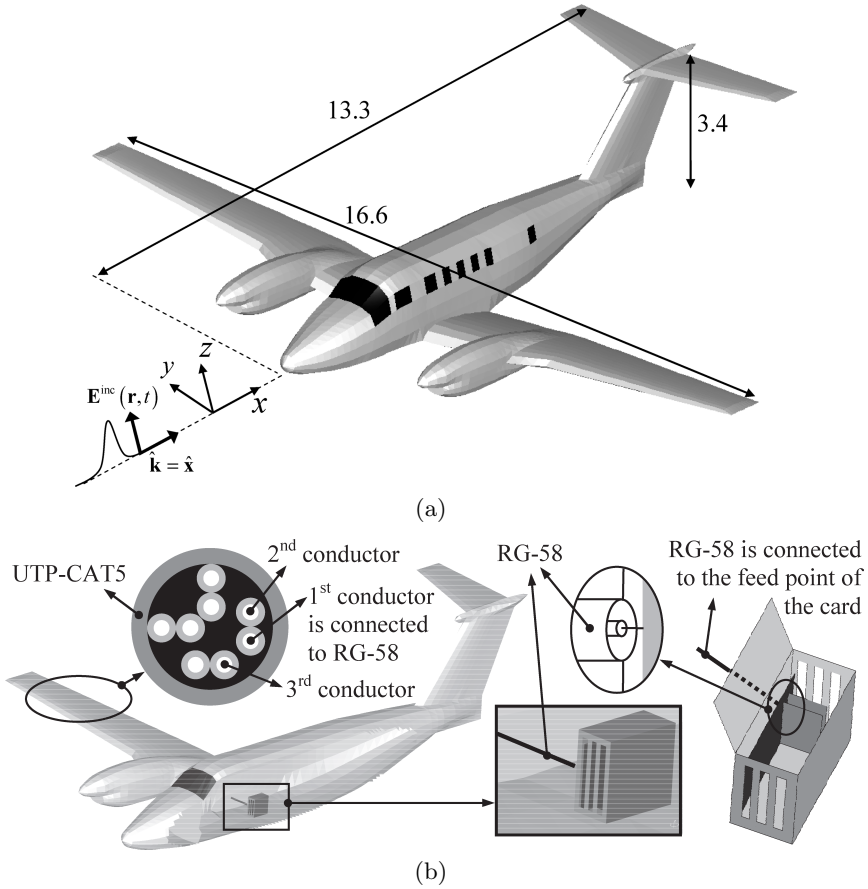

Fig. 3.18. RG-58 and UTP-CAT5 cables on an aircraft. (**a**) Dimensions of the aircraft and the plane-wave excitation. (All dimensions are in meters.) (**b**) Description of the cable-cable-card connections

RG-58 coaxial cable connects the feed pin of the PC's second daughter card and the first conductor of the 5 m long UTP-CAT5 cable located inside the wing cavity (Fig. 3.18b). The PC box enclosing the card configuration has six ventilation slots permitting the interaction of external fields with the card configuration. The UTP-CAT5 cable consists of four pairs of dielectric-coated conductors, which are held together by a dielectric cable jacket. The cable's per-unit-length parameters were extracted using a 2D MOM solver [80] and detailed in [81]. The exposed RG-58 coaxial cable interacts with the external fields via its terminations and along its shield while the UTP-CAT5 cable is embedded within the wing cavity and interacts with the external fields only via its terminations. All UTP-CAT5 cable's conductors (except the first conductor, which is connected to the RG-58 cable) are terminated with 50-Ω

resistors. The structure is illuminated by a plane wave incident on the nose of the aircraft with $E_0 = 3,000\ \mathrm{V\,m^{-1}}$, $\hat{\mathbf{k}} = \hat{\mathbf{x}}$, $\hat{\mathbf{p}} = \hat{\mathbf{z}}$, $f_{\min} = 20$ MHz, $f_c = 135$ MHz, and $f_{\max} = 250$ MHz (Fig. 3.18b). The simulation is carried out for $N_t = 1500$ time steps with $\Delta t = 0.3$ ns. The current density on the surfaces modeling the aircraft, the PC, the card configuration, the coaxial cable and the voltages on the cable loads are modeled by 45 175 surface, 23 wire, 64 junction basis functions and 20 circuit unknowns, respectively. The number of cable unknowns is 18 (2 for the RG-58 and 16 for the UTP-CAT5). Coupling of the external and guided fields (of the RG-58 cable) is realized at 10 points. The temporal basis functions used for discretizing the 3D and 1D TDIEs are prolate-based band-limited interpolant with $8\Delta t$ half-width [9, 10] and third-order Lagrange polynomial [7], respectively. The TD-AIM kernel matches up to fifth-order moments, $\gamma = 5$, $\Delta s_x = 10.52\,\mathrm{cm}$, $\Delta s_y = 9.59\,\mathrm{cm}$, and $\Delta s_z = 10.52\,\mathrm{cm}$; this choice of TD-AIM parameters results in $N_c = 135 \times 180 \times 42$ auxiliary grid points. Figure 3.19a,b present the transient coupled voltages at the source-end terminations of the UTP-CAT5's second and third conductors due to the plane wave excitation. Figure 3.20a–d present snapshots of the current density on the surfaces modeling the aircraft, the PC box, the card configuration, and the coaxial cable at different time

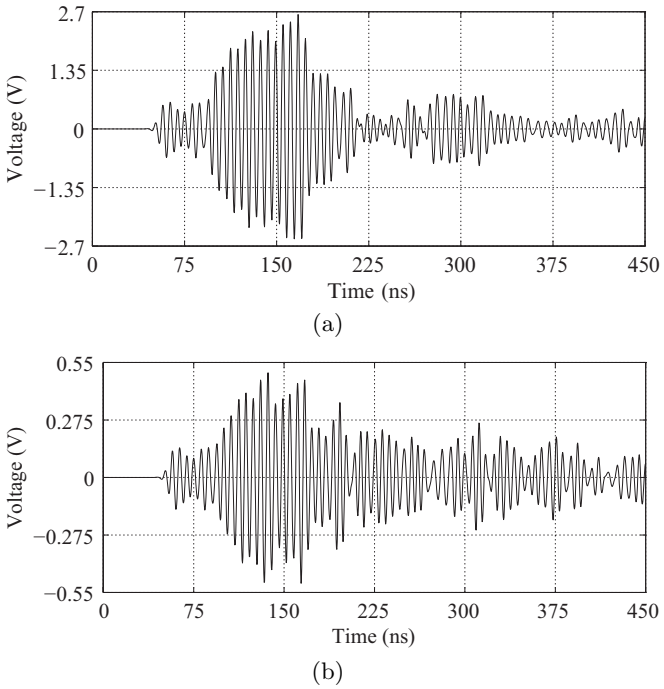

Fig. 3.19. Transient voltages at the source-end terminations of the UTP-CAT5 cable's (**a**) second and (**b**) third conductors

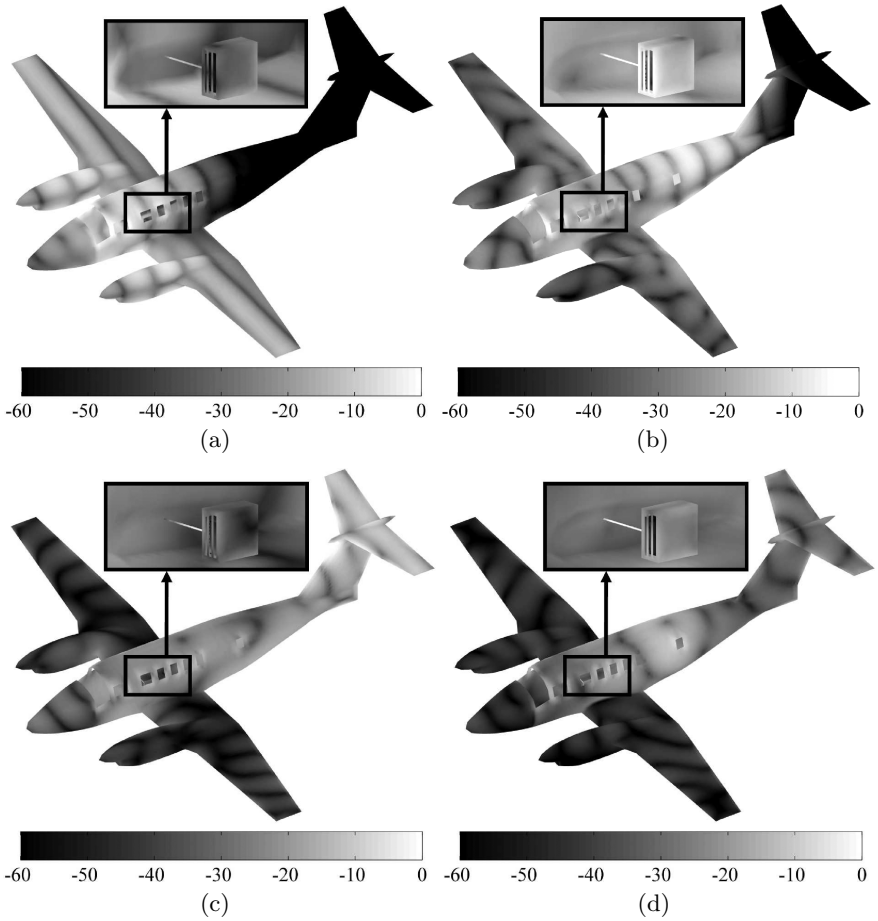

Fig. 3.20. Snapshots of the transient currents on the surfaces modeling the aircraft, the PC box, the card configuration, and the coaxial cable (in dB scale) at (**a**) $\Delta t = 45\,\text{ns}$, (**b**) $\Delta t = 60\,\text{ns}$, (**c**) $\Delta t = 75\,\text{ns}$, and (**d**) $\Delta t = 90\,\text{ns}$

instances. The hybrid simulator required 70 GB of memory and 30 m to fill the matrices and 2.85 h to find the solution using 46 (45 for the field solver, 1 for the circuit and cable solvers) processors.

3.5 Conclusions

This chapter presented a review of progress in fast MOT-TDIE solver technologies for analyzing electromagnetic transients with a specific focus on the application of TD-AIM accelerators. A parallel version of the TD-AIM accelerated MOT-TDIE solver that was hybridized with circuit, cable, and

macromodel simulators was applied to several real-world EMI problems. Our simulations demonstrate that MOT-TDIE solvers are approaching a stage of maturity and becoming an appealing alternative to finite difference/element based simulation technologies.

Acknowledgments

The authors would like to thank the Computational Science and Engineering (CSE) Department at the University of Illinois at Urbana-Champaign for the access to their parallel computer cluster. This work was supported in part by the MURI Grant 2003-07178-01-11, "Modeling antenna feeds," by the DARPA Grant FA9550-06-1-0251, by the AFRL/DE SBIR grant "Time-domain BLT solver for electromagnetic coupling to cables and circuits," and by the CSE fellowship at the University of Illinois.

References

[1] A. Taflove and S. C. Hagness. *Computational Electrodynamics: The Finite-Difference Time-Domain Method*. Artech House, Boston, 2000.

[2] J. Jianming. *The Finite Element Method in Electromagnetics*. Wiley, New York, 2002.

[3] E. K. Miller. A selective survey of computational electromagnetics. *IEEE Trans. Antennas Propagat.*, 36(9):1281–1305, 1988.

[4] A. F. Peterson, L. R. Scott, and R. Mittra. *Computational Methods for Electromagnetics*. Wiley, New York, 1997.

[5] A. Sadigh and E. Arvas. Treating the instabilities in marching on-in-time method from a different perspective. *IEEE Trans. Antennas Propagat.*, 41(12):1695–1702, 1993.

[6] P. J. Davies and D. B. Duncan. Averaging techniques for time-marching schemes for retarded potential integral equations. *Appl. Numer. Math.*, 23:291–310, 1997.

[7] G. Manara, A. Monorchio, and R. Reggiannini. A space-time discretization criterion for a stable time-marching solution of the electric field integral equation. *IEEE Trans. Antennas Propagat.*, 45(3):527–532, 1997.

[8] S. Dodson, S. P. Walker, and M. J. Bluck. Implicitness and stability of time domain integral equation scattering analyses. *ACES J.*, 13(3): 291–301, 1998.

[9] D. S. Weile, G. Pisharody, N. W. Chen, B. Shanker, and E. Michielssen. A novel scheme for the solution of the time-domain integral equations of electromagnetics. *IEEE Trans. Antennas Propagat.*, 52(1):283–295, 2004.

[10] R.A. Wildman, G. Pisharody, D.S. Weile, S. Balasubramaniam, and E. Michielssen. An accurate scheme for the solution of the time-domain integral equations of electromagnetics using higher order vector bases

and bandlimited extrapolation. *IEEE Trans. Antennas Propagat.*, 52 (11):2973–2984, 2004.

[11] T. Abboud, J. C. Nédélec, and J. Volakis. Stable solution of retarded potential equations. In *ACES Conf.*, volume 1, pages 146–151, 2001.

[12] K. Cools, F. P. Andriulli, and E. Michielssen. Time-domain Calderón identities and preconditioning of the time-domain EFIE. In *IEEE AP-S. Int. Symp.*, pages 2975–2978, 2006.

[13] F. P. Andriulli, H. Bağcı, F. Vipiana, G. Vecchi, and Michielssen E. A marching-on-in-time hierarchical scheme for the time domain electric field integral equation. *submitted for publication*, 2007.

[14] A. A. Ergin, B. Shanker, and E. Michielssen. The plane-wave time-domain algorithm for the fast analysis of transient wave phenomena. *IEEE Antennas Propag. Mag.*, 41(4):39–52, 1999.

[15] A. A. Ergin, B. Shanker, and E. Michielssen. Fast analysis of transient acoustic wave scattering from rigid bodies using the multilevel plane wave time domain algorithm. *J. Acous. Soc. Am.*, 107(3):1168–1178, 2000.

[16] B. Shanker, A. A. Ergin, M. Lu, and E. Michielssen. Fast analysis of transient electromagnetic scattering phenomena using the multilevel plane wave time domain algorithm. *IEEE Trans. Antennas Propagat.*, 51(3): 628–641, 2003.

[17] A. E. Yılmaz, J.-M. Jin, and E. Michielssen. Time domain adaptive integral method for surface integral equations. *IEEE Trans. Antennas Propagat.*, 52(10):2692–2708, 2004.

[18] Q. Chen, M. Lu, and E. Michielssen. Integral-equation-based analysis of transient scattering from surfaces with an impedance boundary condition. *Microwave Opt. Tech. Lett.*, 42(3):213–220, 2004.

[19] H. Bağcı, A. E. Yılmaz, V. Lomakin, and E. Michielssen. Fast and accurate solution of time domain electric field integral equation for dielectric half-space. In *IEEE AP-S. Int. Symp.*, volume 3, pages 583–586, 2003.

[20] H. Bağcı, A. E. Yılmaz, V. Lomakin, and E. Michielssen. Fast solution of mixed-potential time-domain integral equations for half-space environments. *IEEE Trans. Geosci. Remote Sensing*, 43(2):269–279, 2005.

[21] N. T. Gres, A. A. Ergin, and E. Michielssen. Volume-integral-equation-based analysis of transient electromagnetic scattering from three-dimensional inhomogeneous dielectric objects. *Radio Sci.*, 36(3): 379–386, 2001.

[22] B. Shanker, A. A. Ergin, and E. Michielssen. Plane-wave-time-domain-enhanced marching-on-in-time scheme for analyzing scattering from homogeneous dielectric structures. *J. Opt. Soc. Am.*, 19(4):716–726, 2002.

[23] G. Kobidze, J. Gao, B. Shanker, and E. Michielssen. A fast time domain integral equation based scheme for analyzing scattering from dispersive objects. *IEEE Trans. Antennas Propagat.*, 53(3):1215–1226, 2005.

[24] K. Aygün, S. E. Fisher, A. A. Ergin, B. Shanker, and E. Michielssen. Transient analysis of multielement wire antennas mounted on arbitrarily shaped perfectly conducting bodies. *Radio Sci.*, 34(4):225–232, 1999.

[25] H. Bağcı, A. E. Yılmaz, J. M. Jin, and E. Michielssen. Fast and rigourous analysis of EMC/EMI phenomena on electrically large and complex cable-loaded structures. *accepted for publication in IEEE Trans. Electromagn. Compat.*, 2006.

[26] K. Aygün, B. C. Fischer, J. Meng, B. Shanker, and E. Michielssen. A fast hybrid field-circuit simulator for transient analysis of microwave circuits. *IEEE Trans. Microwave Theory Tech.*, 52(2):573–583, 2004.

[27] A. E. Yılmaz, J. M. Jin, and E. Michielssen. A parallel FFT accelerated transient field-circuit simulator. *IEEE Trans. Microwave Theory Tech.*, 53(9):2851–2865, 2005.

[28] H. Bağcı, A. E. Yılmaz, and E. Michielssen. EMC/EMI analysis of electrically large and multiscale structures loaded with coaxial cables by a hybrid TDIE-FDTD-MNA approach. In *IEEE AP-S. Int. Symp.*, volume 2B, pages 14–17, 2005.

[29] H. Bağcı, A. E. Yılmaz, and E. Michielssen. A fast hybrid TDIE-FDTD-MNA scheme for analyzing cable-induced transient coupling into shielding enclosures. In *IEEE Int. Symp. EMC*, volume 3, pages 828–833, 2005.

[30] H. Bağcı, A. E. Yılmaz, and E. Michielssen. FFT-accelerated MOT-based solution of time-domain BLT equations. In *IEEE AP-S. Int. Symp.*, pages 1175–1184, 2006.

[31] H. Bağcı, A. E. Yılmaz, and E. Michielssen. Full TDIE-based modeling of electromagnetic coupling into lossy multiconductor cables on electrically large platforms. In *USNC/URSI National Radio Sci. Meet.*, 2005.

[32] A. E. Yılmaz, M. J. Choi, A. C. Cangellaris, J.-M. Jin, and E. Michielssen. Incorporation of frequency-dependent multiport macromodels into a fast time-domain integral equation solver. In *IEEE AP-S. Int. Symp.*, volume 3A, pages 151–154, 2005.

[33] I. Terrasse. *Résolution mathématique et numérique des équations de Maxwell instationnaires par une méthode de potentiels retardés.* PhD thesis, Ècole Polytechnique, 1993.

[34] T. Ha-Duong. On retarded potential boundary integral equations and their discretisation. In M. Ainsworth, P. J. Davies, D. B. Duncan, P.A. Martin, and B.P. Rynne, editors, *Topics in Computational Wave Propagation: Direct and Inverse Problems*, pages 301–336. Springer, Berlin, 2003.

[35] E. Bleszynski, M. Bleszynski, and T. Jaroszewic. AIM:Adaptive integral method for solving large-scale electromagnetic scattering and radiation problems. *Radio Sci.*, 31(5):1225–1251, 1996.

[36] J. R. Phillips and J. K. White. A precorrected-FFT method for electrostatic analysis of complicated 3D structures. *IEEE Trans. Computer-Aided Design*, 16(10):1059–1072, 1997.

[37] V. Rokhlin. Diagonal forms of translational operators for the Helmholtz equation in three dimensions. *Appl. Comput. Harmon. Anal.*, 1(1):82–93, 1993.

[38] V. Rokhlin. Rapid solution of integral equations of classical potential theory. *J. Comp. Phys.*, 60(2):187–207, 1985.

[39] J. M. Song and W. C. Chew. Multilevel fast-multipole algorithm for solving combined field integral equations of electromagnetic scattering. *Microwave Opt. Tech. Lett.*, 10(1):14–19, 1995.

[40] W. C. Chew, J. M. Jin, C. C. Lu, E. Michielssen, and J. M. Song. Fast solution methods in electromagnetics. *IEEE Trans. Antennas Propagat.*, 45(3):533–543, 1997.

[41] M. F. Catedra, R. F. Torres, J. Basterrechea, and E. Gago. *The CG-FFT Method: Application of Signal Processing Techniques to Electromagnetics*. Artech House, Norwood, MA, 1995.

[42] O. P. Bruno. Fast, high-order, high-frequency accurate Fourier methods for scattering problems. In *IEEE AP-S. Int. Symp.*, volume 3, pages 180–183, 2002.

[43] O. P. Bruno and L. A. Kunyansky. A fast, high-order algorithm for the solution of surface scattering problems: basics implementation, tests, and applications. *J. Comp. Phys.*, 169(1):80–110, 2001.

[44] H. T. Anastassiu, M. Smelyanskiy, S. Bindiganavale, and J. L. Volakis. Scattering from relatively flat surfaces using the adaptive integral method. *Radio Sci.*, 33(1):7–16, 1998.

[45] R. F. Bloemenkamp and P. M. Van Den Berg. A conjugate gradient FFT method for transient scattering by dielectric cylinders. In *IEEE AP-S. Int. Symp.*, volume 2, pages 1374–1377, 1999.

[46] A. E. Yılmaz, D. S. Weile, J. M. Jin, and E. Michielssen. A fast Fourier transform accelerated marching-on-in-time algorithm for electromagnetic analysis. *Electromagn.*, 21(3):181–197, 2001.

[47] J. L. Hu, C. H. Chan, and Y. Xu. A fast solution of time domain integral equation using fast Fourier transformation. *Microwave Opt. Tech. Lett.*, 25(3):172–175, 2000.

[48] A. E. Yılmaz, D. S. Weile, J. M. Jin, and E. Michielssen. A hierarchical FFT algorithm (HIL-FFT) for the fast analysis of transient electromagnetic scattering phenomena. *IEEE Trans. Antennas Propagat.*, 50(7): 971–982, 2002.

[49] A. E. Yılmaz, K. Aygün, J. M. Jin, and E. Michielssen. Matching criteria and the accuracy of time domain adaptive integral method. In *IEEE AP-S. Int. Symp.*, volume 2, pages 166–169, 2002.

[50] A. E. Yılmaz, K. Aygün, J. M. Jin, and E. Michielssen. Fast analysis of heatsink emissions with time-domain AIM. In *IEEE Int. Symp. EMC*, Istanbul, Turkey, 2003.

[51] A. E. Yılmaz, J. M. Jin, and E. Michielssen. Time domain adaptive integral method for the combined field integral equation. In *IEEE AP-S. Int. Symp.*, volume 3, pages 543–546, 2003.

[52] A. E. Yılmaz, S. Q. Li, J. M. Jin, and E. Michielssen. A parallel framework for FFT-accelerated time-marching algorithms. In *USNC/URSI National Radio Sci. Meet.*, page 319, 2002.

[53] A. E. Yılmaz, D. S. Weile, B. Shanker, J. M. Jin, and E. Michielssen. Fast analysis of transient scattering in lossy media. *IEEE Antennas Wireless Propagat. Lett.*, 1(1):14–17, 2002.

[54] E. Bleszynski, M. Bleszynski, and T. Jaroszewicz. A new fast time domain integral equation solution algorithm. In *IEEE AP-S. Int. Symp.*, volume 4, pages 176–179, 2001.

[55] A. F. Peterson. The interior resonance problem associated with surface integral equations of electromagnetics: numerical consequences and a survey of remedies. *Electromagn.*, 10(3):293–312, 1990.

[56] B. Shanker, A. A. Ergin, K. Aygün, and E. Michielssen. Analysis of transient electromagnetic scattering from closed surfaces using the combined field integral equation. *IEEE Trans. Antennas Propagat.*, 48(7): 1064–1074, 2000.

[57] S. M. Rao, D. R. Wilton, and A. W. Glisson. Electromagnetic scattering by surfaces of arbitrary shape. *IEEE Trans. Antennas Propagat.*, 30(3): 409–418, 1982.

[58] R. D. Graglia, D. R. Wilton, and A. F. Peterson. Higher order interpolatory vector bases for computational electromagnetics. *IEEE Trans. Antennas Propagat.*, 45(3):329–342, 1997.

[59] C. L. Bennett and H. Mieras. Time-domain scattering from open thin conducting surfaces. *Radio Sci.*, 10(6):1231–1239, 1981.

[60] E. Topsakal, M. Carr, J. Volakis, and M. Blezsynski. Galerkin operators in adaptive integral method implementations. *Proc. Microwaves Antennas Propagat.*, 148(2):79–84, 2001.

[61] X. C. Nie, L. W. Li, and N. Yuan. Precorrected-FFT algorithm for solving combined field integral equations in electromagnetic scattering. In *IEEE AP-S. Int. Symp.*, volume 3, pages 574–577, 2002.

[62] F. Ling, C. F. Wang, and J. M. Jin. Application of adaptive integral method to scattering and radiation analysis of arbitrarily shaped planar structures. *J. Electromagn. Waves Appl.*, 12(8):1021–1037, 1998.

[63] E. Hairer, C. H. Lubich, and M. Schlichte. Fast numerical solution of nonlinear Volterra convolution equations. *SIAM J. Sci. Stat. Comput.*, 6(3):532–541, 1985.

[64] M. Frigo and S. G. Johnson. FFTW: An adaptive software architecture for the FFT. In *IEEE ICASSP*, volume 3, pages 1381–1384, 1998.

[65] S. P. Walker and C. Y. Leung. Parallel computation of time-domain integral equation analyses of electromagnetic scattering and RCS. *IEEE Trans. Antennas Propagat.*, 45(4):614–619, 1997.

[66] C.-W. Ho, A. Ruehli, and P. Brennan. The modified nodal approach to network analysis. *IEEE Trans. Circuits Syst.*, 22(6):504–509, 1975.

[67] L. Kijun and S.-Bai Prak. Reduced modified nodal approach to circuit analysis. *IEEE Trans. Circuits Syst.*, 32(10):1056–1060, 1985.

[68] A. Vladimirescu. *The Spice Book*. Wiley, New York, 1994.

[69] C. R. Paul. *Analysis of Multiconductor Transmission Lines*. Wiley, New York, 1994.

[70] F. Olyslager. *Electromagnetic Waveguides and Transmission Lines*. Oxford University Press, Oxford, U.K., 1999.

[71] N. B. Rabbat, Ruehli A. E., Mahoney G. W., and Coleman J. J. A survey on macromodeling. In *IEEE Int. Symp. Circuits Syst.*, 1975.

[72] N. B. Rabbat, Ruehli A. E., Mahoney G. W., and Coleman J. J. A review of macromodeling techniques. *IEEE Circuit Syst. Newsletter*, 9: 3–9, 1975.

[73] A. Semlyen and A. Dabuleanu. Fast and accurate switching transient calculations on transmission lines with ground return using recursive convolution. *IEEE Trans. Power Appar. Syst.*, 94(2):561–571, 1975.

[74] W. Janke and G. Blakiewicz. Semi-analytical recursive algorithms for convolution calculations. *IEE Proc.-Circuit Devices Syst.*, 42(2):125–130, 1995.

[75] T. Hu, B. Zhong, S. L. Dvorak, and J. L. Prince. Application of recursive convolution to transient simulation of interconnects using a hybrid phase-pole macromodel. *IEEE Trans. Adv. Pack.*, 27(4):603–610, 2004.

[76] A. C. Cangellaris, M. Celik, S. Pasha, and L. Zhao. Electromagnetic model order reduction for system-level modeling. *IEEE Trans. Microwave Theory Tech.*, 47(6):840–850, 1999.

[77] A. C. Cangellaris and L. Zhao. Model order reduction techniques for electromagnetic macromodelling based on finite methods. *Int. J. Num. Modeling: Electronic Networks, Devices and Fields*, 3(2-3):181–197, 2000.

[78] E. F. Vance. *Coupling to Shielded Cables*. Wiley, New York, 1978.

[79] K. Aygün, B. Shanker, A. A. Ergin, and E. Michielssen. A two-level plane wave time-domain algorithm for fast analysis of EMC/EMI problems. *IEEE Trans. Electromagn. Compat.*, 44(1):152–164, 2002.

[80] J. C. Clements, C. R. Paul, and A. T. Adams. Computation of the capacitance matrix for systems of dielectric-coated cylindrical conductors. *IEEE Trans. Electromagn. Compat.*, 17(4):238–248, 1975.

[81] P. Kirawanich, N. E. Islam, and S. J. Yakura. An electromagnetic topology approach: Crosstalk characterization of the unshielded twisted-pair cable. *PIER*, 58:285–299, 2006.

http://www.springer.com/978-3-540-73777-3

Modeling and Computations in Electromagnetics
A Volume Dedicated to Jean-Claude Nédélec
Ammari, H. (Ed.)
2008, IX, 235 p., Softcover
ISBN: 978-3-540-73777-3